Nuclear Engineering and Technology 55 (2023) 3164–3182

Contents lists available at ScienceDirect

Nuclear Engineering and Technology

journal homepage: www.elsevier.com/locate/net

Original Article

The DISNY facility for sub-cooled flow boiling performance analysis of CRUD deposited zirconium alloy cladding under pressurized water reactor condition: Design, construction, and operation

Ji Yong Kim, Yunju Lee, Ji Hyun Kim**, In Cheol Bang*

Department of Nuclear Engineering, Ulsan National Institute of Science and Technology (UNIST), 50 UNIST-gil, Ulju-gun, Ulsan, 44919, Republic of Korea

ARTICLE INFO

Article history:
Received 6 January 2023
Received in revised form
8 May 2023
Accepted 2 June 2023
Available online 4 June 2023

Keywords:
CRUD
Fouling
Deposition
Subcooled nucleate boiling
PWR
DISNY

ABSTRACT

The CRUD on the fuel cladding under the pressurized water reactor (PWR) operating condition causes several issues. The CRUD can act as thermal resistance and increases the local cladding temperature which accelerate the corrosion process. The hideout of boron inside the CRUD results in axial offset anomaly and reduces the plant's shutdown margin. Recently, there are efforts to revise the acceptance criteria of emergency core cooling systems (ECCS), and additionally require the modeling of the thermal resistance effect of the CRUD during the performance analysis. There is an urgent need for the evaluation of the effect of the CRUD deposition on the cladding heat transfer under PWR operating conditions, but the experimental database is very limited. The experimental facility called DISNY was designed and constructed to analyze the CRUD-related multi-physical phenomena, and the performance analysis of the constructed DISNY facility was conducted. The thermal-hydraulic and water chemistry conditions to simulate the CRUD growth under PWR operating conditions were established. The design characteristics and feasibility of the DISNY facility were validated by the MARS-KS code analysis and separate performance tests. In the current study, detailed design features, design validation results, and future utilization plans of the proposed DISNY facility are presented.

1. Introduction

The CRUD (Chalk River Undenied Deposit or Corrosion Related Unidentified Deposit) is a fouling deposit usually found on the nuclear fuel cladding in a light water-cooled reactor (LWR). The CRUD mainly takes the form of porous structures with a submicron scale pore, and thickness of several tens of micrometers up to ~100 μm [1–3]. The CRUD is characterized by having a steam chimney with a few micron diameters within a porous matrix. The CRUD is mainly composed of metal oxide corrosion products from the reactor coolant systems such as nickel oxide (NiO), and nickel ferrite ($NiFe_2O_3$). The CRUD is mainly formed by the deposition of these corrosion products during the subcooled boiling process that occurred at the upper span region of the fuel assembly [4] as depicted in Fig. 1. The subcooled nucleate boiling (SNB) on the fuel cladding surface was pointed out as a key factor of multi-physical phenomena related to the CRUD from the previous literature [5–14].

The deposition of CRUD under pressurized water reactor (PWR) conditions raises several operational and safety-related issues [15]. The AOA (Axial Offset Anomaly) occurred by the accumulation of boron inside the CRUD is one of the problems related to the CRUD. The concentrated boron inside the CRUD shifts the power distribution toward the bottom of the reactor core and reduces the shutdown margin of the reactor. Reduced shutdown margin requires a decrease of the reactor power level down to ~70% [16]. and deteriorates the economics of the power plants. The CILC (CRUD Induced Localized Corrosion) is another issue related to the CRUD. The deposition of the thick, porous CRUD layer acts as an additional thermal barrier and increases the local cladding temperature. The increased cladding temperature accelerates the corrosion of the cladding and can lead to fuel failure [3]. The enhancement of the PWR performance or the economics is limited by the existence of the CRUD [5]. The uprating of the power level or the utilization of the high burnup fuel intensifies the degree of the subcooled boiling level and accelerates the growth of the CRUD [1] which results in the increased potential risk of the AOA and CILC occurrence.

* Corresponding author.
** Corresponding author.
E-mail addresses: kimjh@unist.ac.kr (J.H. Kim), icbang@unist.ac.kr (I.C. Bang).

https://doi.org/10.1016/j.net.2023.06.006

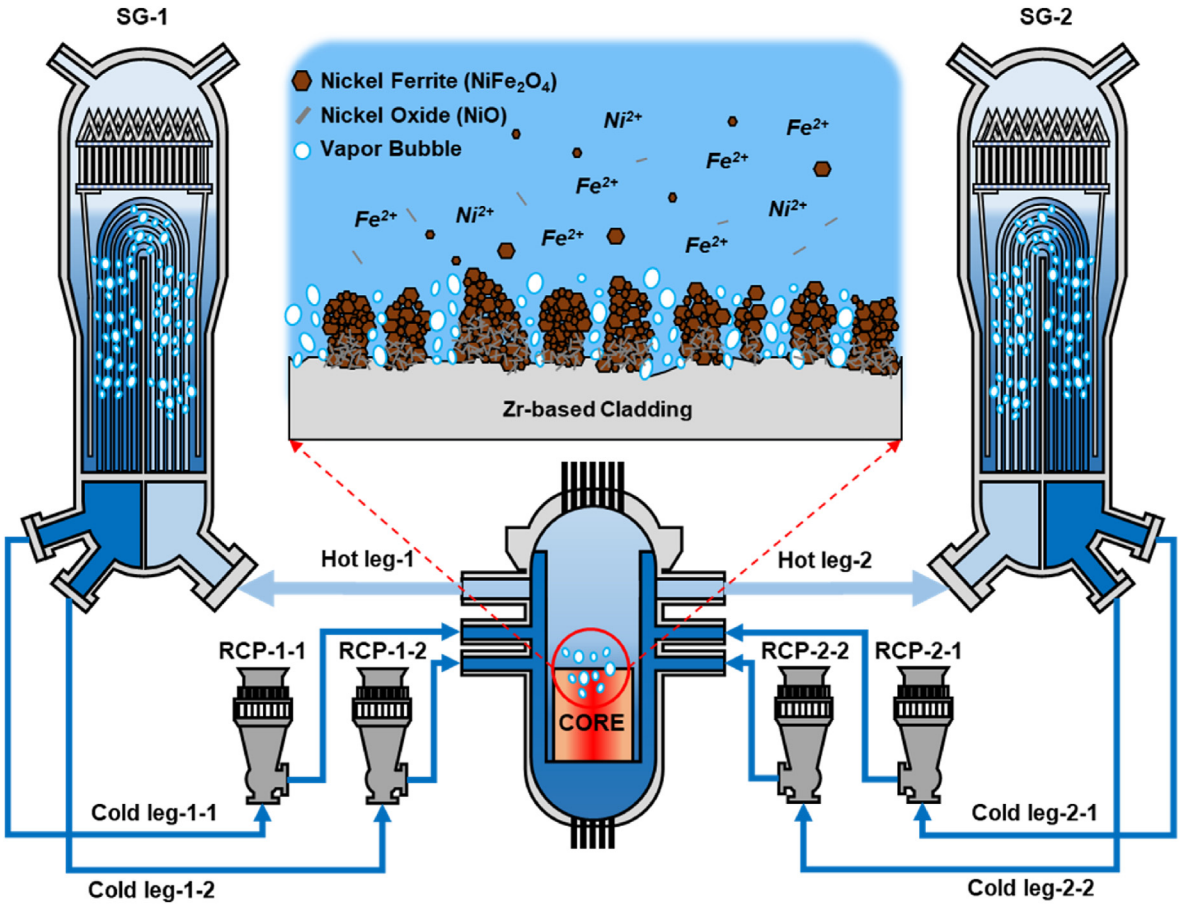

Fig. 1. Schematics of the CRUD deposition behavior under PWR operation conditions.

Furthermore, the acceptance criteria for the PWR plant emergency core cooling system are expected to be revised in the US (NRC; 10 CFR 50.46c) and the Republic of Korea (NSSC; Notice No. 2017-23) to reflect the effect of high-burnup fuel. The revised ECCS acceptance criteria draft additionally requires the modeling of the CRUD thermal resistance effect during the evaluation of the ECCS performance. There are urgent needs for the development of precise and accurate CRUD-related phenomena analysis tools during both PWR normal and accidental conditions.

Attempts were made to implement the effect of CRUD deposition on the reflooding heat transfer during LOCA (Loss of Coolant Accident) with the safety analysis code. Hu et al. analyzed the effect of thermal resistance of the CRUD layer with constant thermal conductivity (0.8648W/m-K) on LOCA of Westinghouse four-loop PWR with RELAP5-3D [17]. Lee et al. investigated the thermal resistance effect of the CRUD with simplified CRUD effective thermal conductivity model on the LOCA of ARP-1400 reactor with FRAPTRAN-2.0 KS code [18]. The safety analysis with the consideration of CRUD thermal resistance showed the increased peak cladding temperature during blowdown and the reflood phase of the LOCA due to the additional thermal resistance of the CRUD. However, the assumption of constant thermal conductivity or the simplified effective thermal conductivity model of the CRUD layer does not reflect the enhanced effective thermal conductivity by the initiation of SNB and can result in too far conservative analysis results. Also, various multi-physics computational codes were developed to analyze the heat and mass transfer behavior inside the CRUD. Cohen proposed the wick boiling mechanism to describe the heat and chemical species transport inside the CRUD [6]. The proposed wick boiling model was modified and extended by the following researchers to analyze the AOA and CILC. Pan et al. extend the wick boiling model into the 2-D domain with consideration of chemical species transport with the assumption of infinite soluble solutes (H_3BO_3) [7]. Henshaw et al. refined the chemical model of wick boiling by adopting the detailed chemical reactions that are relevant in crud deposits to analyze the precipitation of the boron in the form of the lithium metaborate ($LiBO_2$) and the bonaccordite (Ni_2FeBO_5) [9]. Haq et al. considered the solute concentration effects on the saturation temperature of the primary coolant [10]. Short et al. developed the multi-physics CRUD boron deposition analysis code called MAMBA-BDM with consideration of the convective heat transfer inside the porous shell region [7]. Yeo and NO proposed the modified wick boiling model with consideration of nucleate boiling at the cladding-CRUD interface instead of evaporative heat transfer at the chimney wall [8]. The validation of the proposed multi-physics model requires the experimental database regarding the geometric or chemical features of the CRUD layer, and the SNB characteristics of the fouled cladding surface under PWR operating conditions. However, the number of experimental works on the CRUD growth simulation and the characterization of the SNB performance on CRUD deposited cladding surface under PWR operation conditions are very limited due to the difficulty of the experiment in high pressure and temperature conditions. Dumnernchanvanit et al. investigated the effect of fouling-resistant coating on CRUD growth under the pressurized condition (11.5 MPa and 320 °C) [19]. The nine different types of materials are coated on the 316 stainless steel surfaces via physical vapor deposition (PVD) and surfaces with TiC and ZrN coating

showed a reduction of CRUD adhesion amount of ~40%. Baek et al. evaluated the effect of the chemical etching of the fuel cladding on the CRUD deposition and SNB behavior in pressurized conditions (13.0 MPa and 328 °C) [20]. The chemical etching increased surface wettability and decreased surface roughness of the cladding and SNB intensity measured by the acoustic emission (AE) sensor was decreased due to the suppressed bubble nucleation. The amount of the CRUD deposit on the etched cladding was reduced by ~51% due to the reduced SNB. Baek et al. analyze the effect of applied heat flux on the CRUD growth under pressurized conditions (13.0 MPa and 325 °C) [21]. The increased applied heat flux increases the SNB intensity which enhances the CRUD growth under pressurized conditions. The SNB characteristics of the CRUD deposited cladding surface under PWR operating conditions were experimentally analyzed in the WALT (Westinghouse Advanced Loop Tester) facility [3,22–24]. The chemical and geometric characteristics of the simulated CRUD were analyzed, and the fouling resistance of the CRUD deposits was quantified. The experimental results show that the fouling resistance of the CRUD was strongly affected by the thickness of the CRUD and applied heat flux which the determines flow regime inside the porous CRUD. Macbeth et al. investigate the effect of CRUD deposits on pressure drop characteristics and the dry-out heat flux of 321 stainless steel rods under heavy water reactor operation conditions [25]. The CRUD deposited rods show ~5–10% reduction in the dry-out heat flux and ~50% increase in two-phase pressure drop compared to the clean rod cases. The experimental condition of the previous experimental studies on the CRUD growth simulation and SNB performance characterization are summarized in Fig. 2. Most of the previous experiments were conducted under reduced pressure and reduced mass flux conditions compared to the typical PWR normal operation conditions (blacked region). It is well known that SNB characteristics are affected by the operating pressure, inlet enthalpy and mass flux conditions. The deviation of the experimental conditions from the typical PWR conditions can cause different SNB behavior on the cladding surface which strongly influence the CRUD growth and fouling resistance characteristics. Also, most of the previous work did not evaluate the SNB characteristics of the CRUD deposited surface except WALT facility under PWR operating condition.

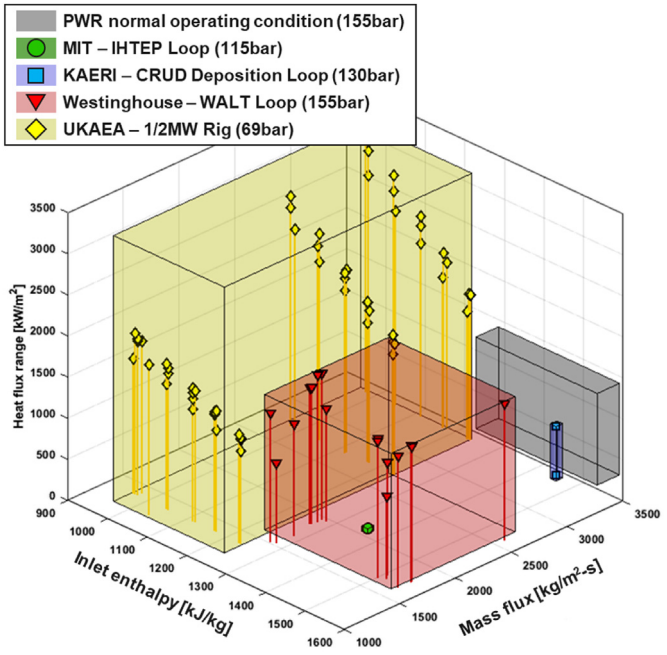

Fig. 2. Summary of experimental conditions of the previous research on CRUD [3,19,21,25].

Furthermore, there are controversial issues about whether the CRUD deposition on the cladding increase or decreases the safety margins of the PWR. Buongiorno outlined the possibility of the enhancement of the PWR safety margin (increase of critical heat flux and Leidenfrost point temperature) with the deposition of CRUD based on the experimental results analysis of the engineered CRUD surfaces under atmospheric pressure conditions [26]. Karoutas et al. investigate the CHF characteristics of the CRUD deposited clean ZIRLO™ cladding and Cr-coated accident tolerant fuel cladding under PWR conditions with the WALT facility [24]. The experimentally measured CHF values between CRUD deposited cladding and clean cladding surface show negligible differences. Modeling the effect of the CRUD deposition on the fuel cladding during the performance or the safety analysis of the PWR requires information regarding the effect of the CRUD on the thermal-hydraulic (TH) characteristics such as single/two-phase heat transfer, and pressure drop. Also, the quantification of the surface characteristics such as morphology, roughness, porosity, chemical composition, wettability, and capillary wicking which strongly affect the boiling heat transfer characteristics (critical heat flux, reflooding, or quenching heat transfer) is strongly needed.

The high-pressure subcooled flow boiling experimental facility called DISNY (crud DeposItion Simulator for Nuclear energY) was designed [27,28] and constructed as a testbed to simulate the CRUD growth and to investigate the SNB heat transfer performance of the CRUD deposited cladding surface under PWR operating conditions. In the current paper, the detailed design features and the design validation works of the DISNY are presented. The established TH and water chemistry experimental conditions and underlying logic and methodology to simulate the PWR operating conditions are provided. The design validation and feasibility analysis of the proposed high-pressure/temperature facility were conducted based on the MARS-KS and preliminary experiments. The future utilization plans of the DISNY facility as an effective means to analyze the CRUD-related multi-physics phenomena such as AOA and CILC are presented.

2. Design features of the DISNY facility

The high-pressure/temperature sub-cooled flow boiling experimental facility called DISNY (crud DeposItion Simulator for Nuclear energY) was designed and constructed to simulate the CRUD growth under PWR normal operating conditions and mainly focused on the SNB characteristics analysis of the CRUD deposited fuel cladding surfaces. The proposed DISNY facility has the unique feature of simulating both the TH and water chemistry experimental environment of a pressurized water reactor to experimentally simulate the CRUD growth on the surface of nuclear fuel cladding. The reference reactor designs of the current DISNY facility are OPR1000 (Optimized Power Reactor 1000) and APR1400 (Advanced Power Reactor 1400) which are the operating PWR in the Republic of Korea. The general design features of the DISNY facility are compared to the reference reactor designs (OPR1000 and APR1400), and the WALT facility which are summarized in Fig. 3 and Table 1 respectively. The operating conditions of DISNY (a violet region in Fig. 3) which include pressure, temperature, mass flux, and heat flux range were established to fully cover the reference reactor's design values to overcome the limitations of the previous experimental studies. The DISNY facility consists of the primary system (PRS) for CRUD growth and SNB performance evaluation and the chemical control system (CCS) for controlling the water chemistry condition. The design features of the DISNY

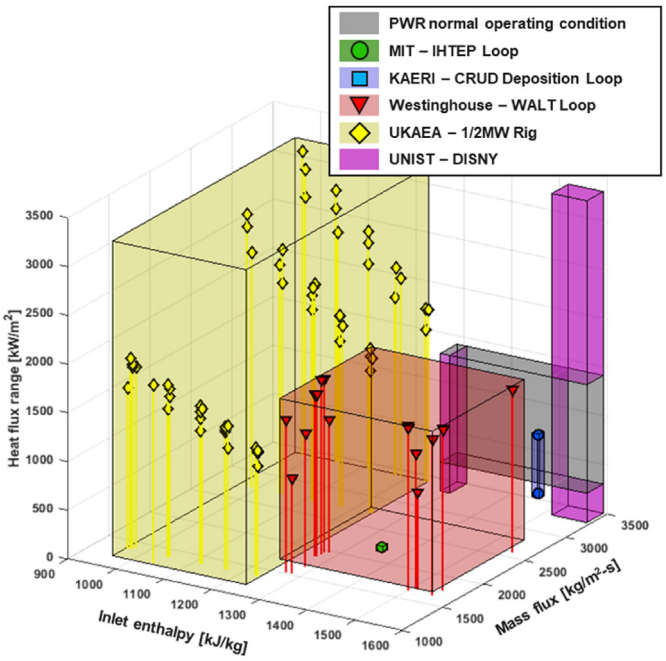

Fig. 3. Comparison of thermal hydraulic experimental conditions of the DISNY.

facility are depicted in Fig. 4 and the constructed DISNY facility is shown in Fig. 5.

2.1. Primary system

The PRS of the DISNY facility simulate the CRUD growth by boiling deposition under SNB conditions and evaluate the fouling resistance of the CRUD under PWR normal operating conditions. The piping and instrumentation diagram of the PRS is shown in Fig. 6, consisting of an autoclave test section (TX), preheater, canned motor main coolant pump (MCP), shell and tube heat exchanger (HX), pressurizer (PZR), and orifice flowmeter. The CRUD growth simulation and the SNB characteristics analysis experiment of the CRUD deposited cladding surface are conducted in an in-situ way to minimize deformation and loss of the simulated CRUD during the experiment.

The PRS is pressurized by the generated steam inside the PZR with aid of immersed cartridge heaters. The TX inlet temperature is controlled by the preheater operation with immersed cartridge heaters. The canned motor pump is utilized as MCP. The fluid control valve (FCV) is located on the bypass line for regulating the mass flux to the TX. The water chemistry conditions of the PRS are controlled by the CCS. The borated working fluid and CRUD deposition precursors are injected into the PRS through the charging line of the CCS. The working fluid inventory of the PRS is controlled by letdown flow rate of letdown line.

2.1.1. Test section design of the DISNY

The autoclave type TX design, which is depicted in Fig. 7, was adopted in DISNY facility to simulate the single sub-channel TH conditions. The annulus-shaped heated channel with Joule heated heater assembly (HTA) with active heating length of 300 mm is used. The required hydraulic diameter to simulate the single sub-channel conditions of the reference plants of the DISNY TX was calculated based on the geometry information of PLUS7 PWR fuel [31] (utilized in OPR1000 and APR1400). The calculated equivalent hydraulic diameter of the PLUS7 fuel single subchannel by Eqn. (1) is 12.6 mm (pin pitch = 12.9 mm, pin diameter = 9.5 mm).

$$D_h = \frac{4 \times A_{channel}}{L_{wet}} = \frac{4p^2 - \pi D_{pin}^2}{\pi D_{pin}} \quad (1)$$

The entrance length of 150 mm ($L/D_h = 11.87$) was considered in the heated section downstream to stabilize the inlet flow conditions of the heated channel. The Al_2O_3 ceramic structures are inserted inside the heated channel to make designated flow channel area while maintaining the electrical insulation conditions with Joule heated heater. The TX inlet (*TX-T-1*), TX inlet plenum (*TX-T-2*), heated channel bulk fluid (*TX-T-3*;150 mm from the bottom of cladding), and TX outlet (*TX-T-4*) fluid temperatures are continuously monitored by k-type TC during the experiment. The TX outlet pressure (*TX-P*) and the heated channel pressure difference (*TX-dP*; between the inlet plenum and TX outlet) are measured by pressure transmitter and differential pressure transmitter respectively.

The U-shaped HTA design (one end is opened) with active heating length of 300 mm was adopted in DISNY facility. The region of interest of the HTA is limited to the 300 mm of the topmost grid span region of the hottest fuel pin where the most active SNB is expected to actively occur [4,16]. The design features of the DISNY HTA are depicted in Fig. 8. The HTA consists of a lead electrode, lower and upper endcap, zirconium-based alloy cladding active heating element, and metallic guide tube elements for the measurement instrumentations. The zirconium-based alloy claddings with OD of 9.5 mm and thickness of 0.6 mm, which are the same material as an actual cladding of PWR, are utilized as a heater surface to minimize the distortion of the physiochemistry reactions of CRUD growth. The two K-types TCs are inserted inside the cladding with aid of Al_2O sleeve to measure the inner wall temperature of middle section of active heating length. The voltage drop across the active heating length is measured by two wires and guided through the metallic guide tube elements. The applied electrical current level of the HTA is measured by shunt resistance.

Table 1
Comparison results of design features of the DISNY and reference reactors.

Parameter	DISNY [27]	WALT [3]	OPR1000 [29]	APR1400 [30]	Unit
Design pressure	20.0	20.7	-	-	[MPa]
Operating pressure	15.5	15.5	15.5	15.5	[MPa]
Design temperature	360	345	-	-	[°C]
Operating temperature	290–340	290–335	296–327	291–325	[°C]
Mass flux	3300-3500	1610-2574	3461-3567	3344-3499	[kg/m²-s]
Test section inlet temperature	290–340	290–335	-	-	[°C]
Maximum heat flux	2300	1537	1331	1413	[kW/m²]
Heater material	Zircaloy-4	ZIRLO™			-
Heater array	Single rod (Annulus flow channel)		17x 17 Square lattice (PLUS 7 fuel assembly)		-
Test section hydraulic diameter	12.64	14.17–14.40	12.64		[mm]

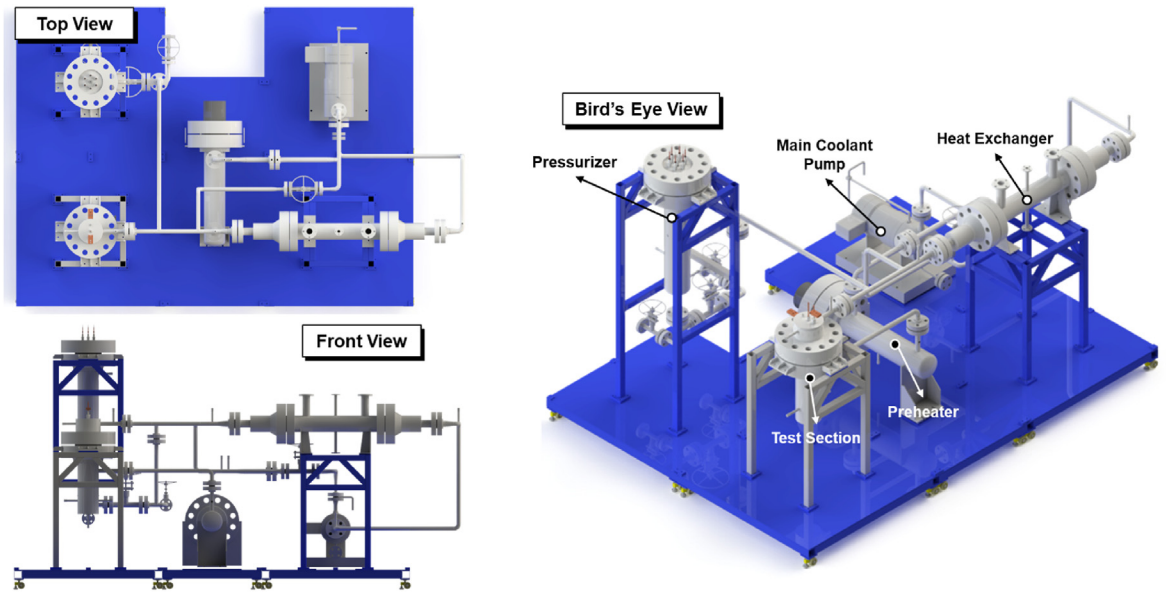

Fig. 4. Schematics on the design features of DISNY facility.

Fig. 5. Photo of the constructed DISNY facility.

2.2. Chemical control system

The CCS of the DISNY maintains the desired water chemistry condition and coolant inventory of the PRS coolant during the experiment. The design features of the CCS can be found in Fig. 9. The CCS consists of the chemical control tank, metal ion storage tank, coolant storage tanks, and various pumps with instrumentations. The water chemistry conditions such as pH, ion-conductivity, DO, and DH are continuously monitored during experiment. The borated water stored inside the coolant storage

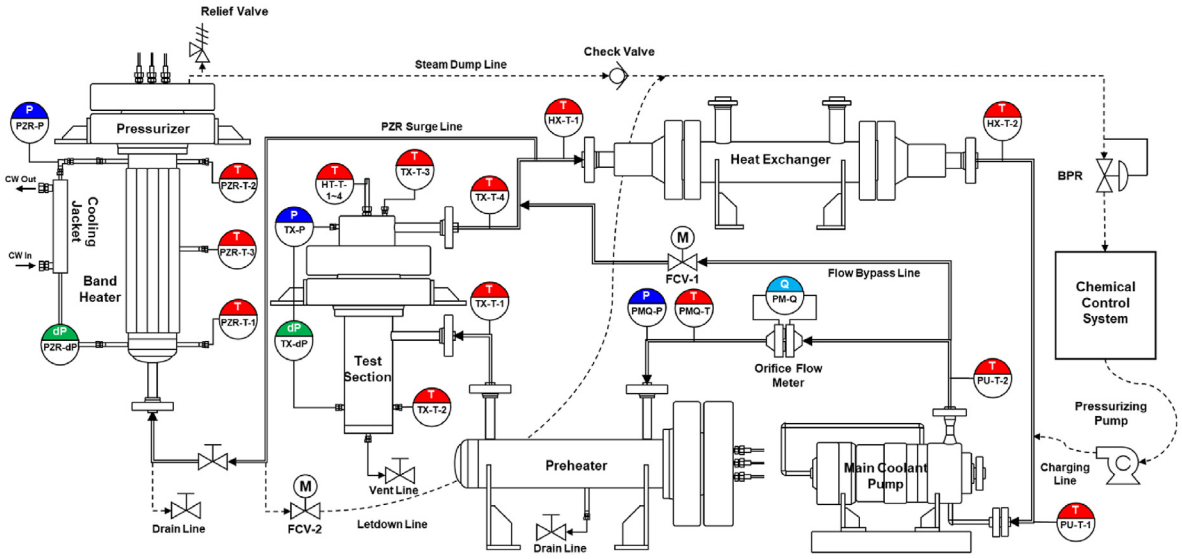

Fig. 6. Primary system P&ID diagram of the DISNY Facility.

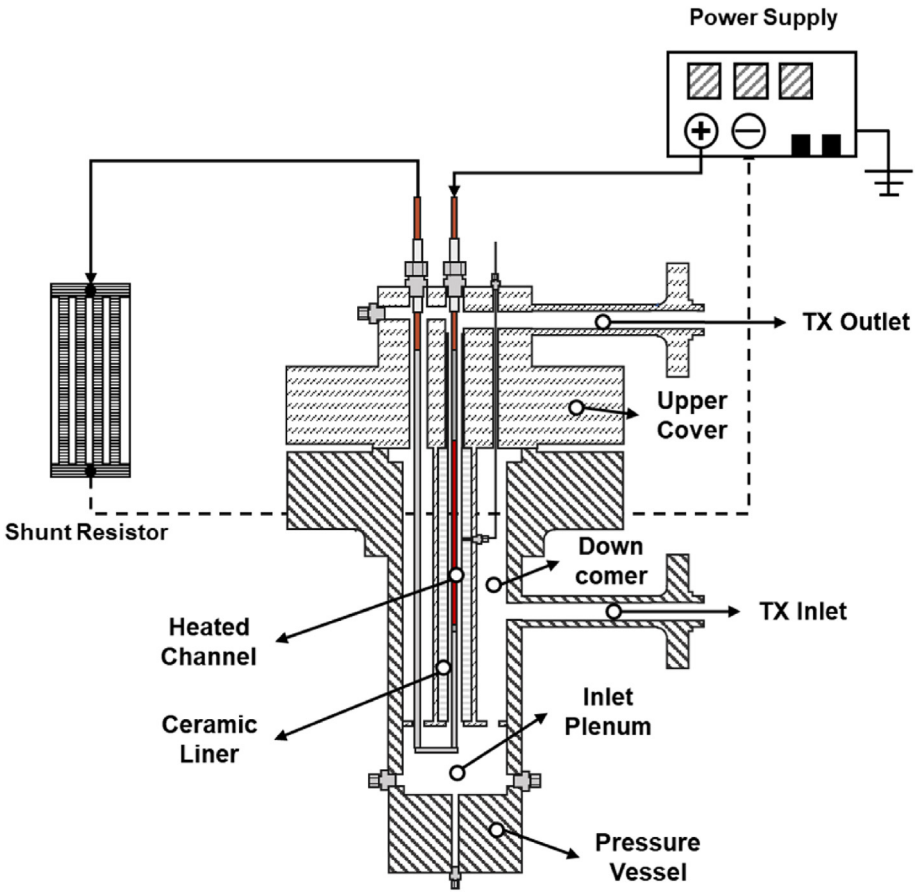

Fig. 7. Schematics of the DISNY test section.

tank is utilized as working fluid and the pH is controlled by the amount of LiOH added to the coolant storage tank. The DO and DH of the DISNY working fluid is controlled by chemical control tank. The Ni and Fe ions, stored inside metal ion storage tank, are used as CRUD precursors in the DISNY facility.

3. Experimental conditions and setup of DISNY facility

3.1. Thermal-hydraulic conditions for sub-cooled boiling experiment

TH experimental conditions of the DISNY facility were

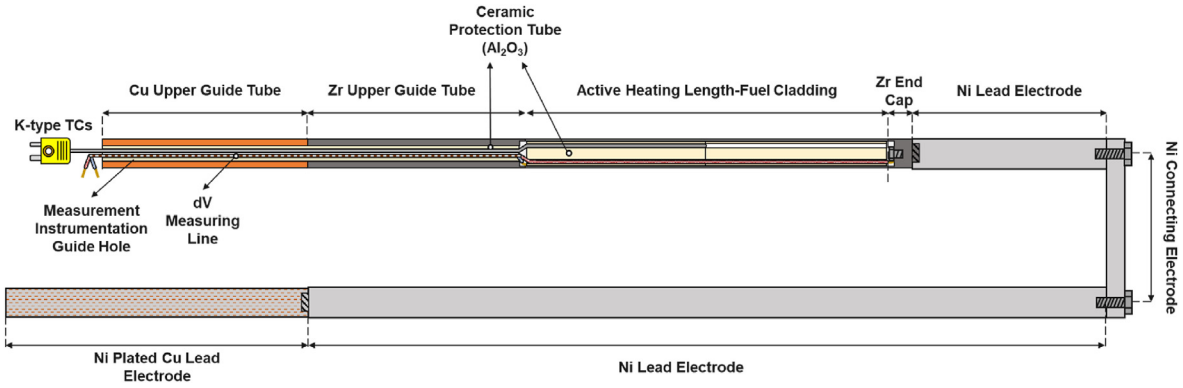

Fig. 8. Design features of the DISNY heater assembly.

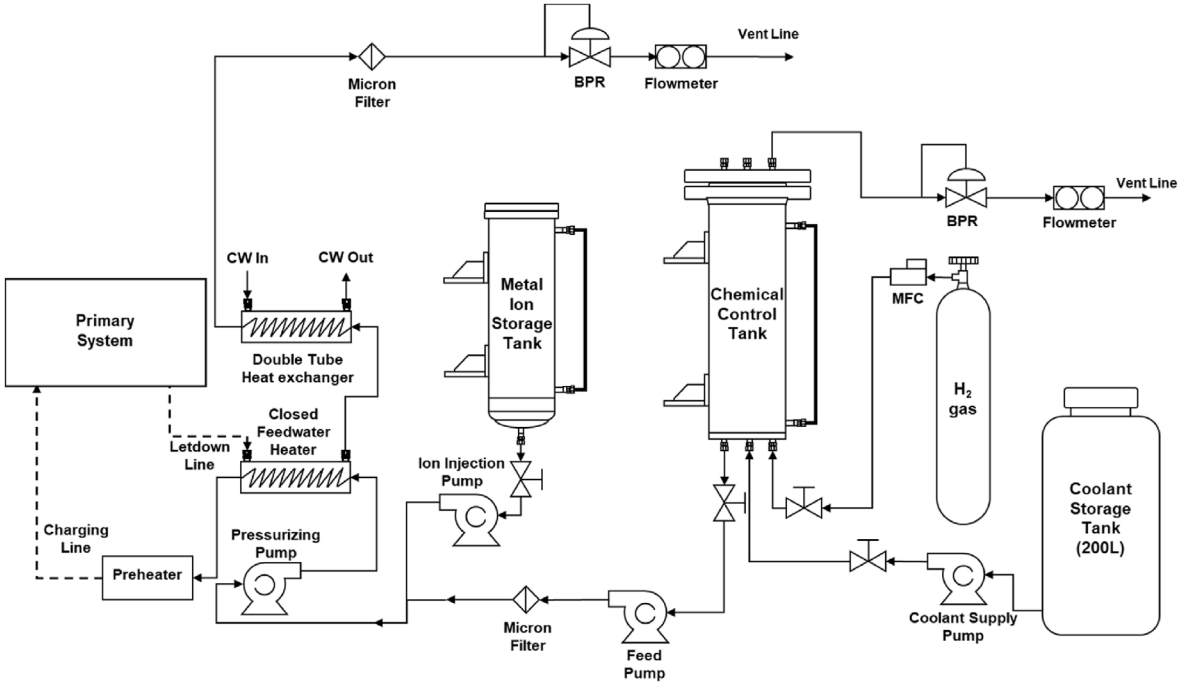

Fig. 9. Chemical control system P&ID diagram of the DISNY facility.

established to simulate the SNB phenomena inside the core. The region of interest was confined to the single sub-channel of the hottest fuel pin where the most vigorous SNB occurrence is expected. The thermal hydraulic conditions inside the hottest fuel pin sub-channel were analyzed by MARS-KS code. The MARS-KS code is the one-dimensional thermal-hydraulic system safety analysis code used developed by KAERI by incorporating the RELAP5/MOD3 and COBRA-TF [32]. The single sub-channel with an active height of 3,810 mm was considered based on the PLUS7 fuel assembly geometry. The schematics of the PLUS7 fuel assembly and the input model for the sub-channel analysis are depicted in Fig. 10 (a) and (b) respectively. The hydraulic model for the single sub-channel was made with pipe components with the equivalent cross-sectional area and hydraulic diameter, and heat structure was added to simulate the hottest fuel pin power. The boundary conditions including inlet temperature, outlet pressure, mass flux, and heat flux profiles were set based on the design values of the OPR1000 [29] and APR1400 [30] final safety analysis report (FSAR). Three representatives heat flux profiles of the reference reactors (OPR1000 and APR1400) were considered in the sub-channel analysis and normalized heat flux profiles are shown in Fig. 10 (c) and (d). The average linear heat generation rate of 17.26 kW/m for OPR100 and 17.91 kW/m for APR1400 was used in the sub-channel analysis, where a radial pin power peaking factor of 1.55 was assumed for the hottest fuel pin.

The single sub-channel analysis results of the OPR1000 and APR1400 hottest fuel pin are shown in Fig. 11 (a) and (b) respectively. The temperature profiles of the coolant and the cladding temperature show different behavior depending on the heat flux profiles. However, the sub-cooled nucleate boiling was observed in the 9th and 10th grid span region of the hottest fuel pin in all cases. The steaming rate [16], defined by Eqn. (2), is used to quantify the vapor generation in single sub-channel analysis. The steaming rate behaviors were different depending on the axial power distribution and the 1.26 peak cases showed the largest steaming rate for both OPR1000 and APR1400 conditions.

$$s = q''_{NB}/l_{lv} \tag{2}$$

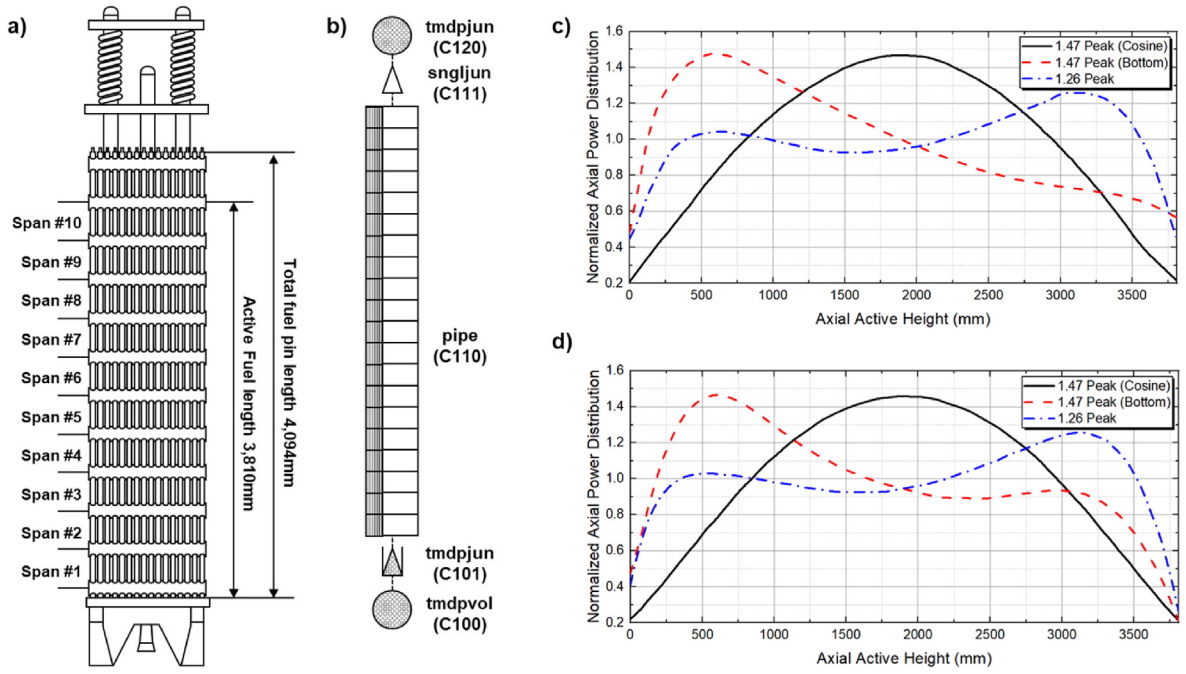

Fig. 10. (a) Schematics of the PLUS7 fuel assembly, (b) MARS-KS nodalization for the hot pin sub-channel analysis, (c) OPR1000 normalized axial power distribution profile [29], (d) APR1400 normalized axial power distribution profile [30].

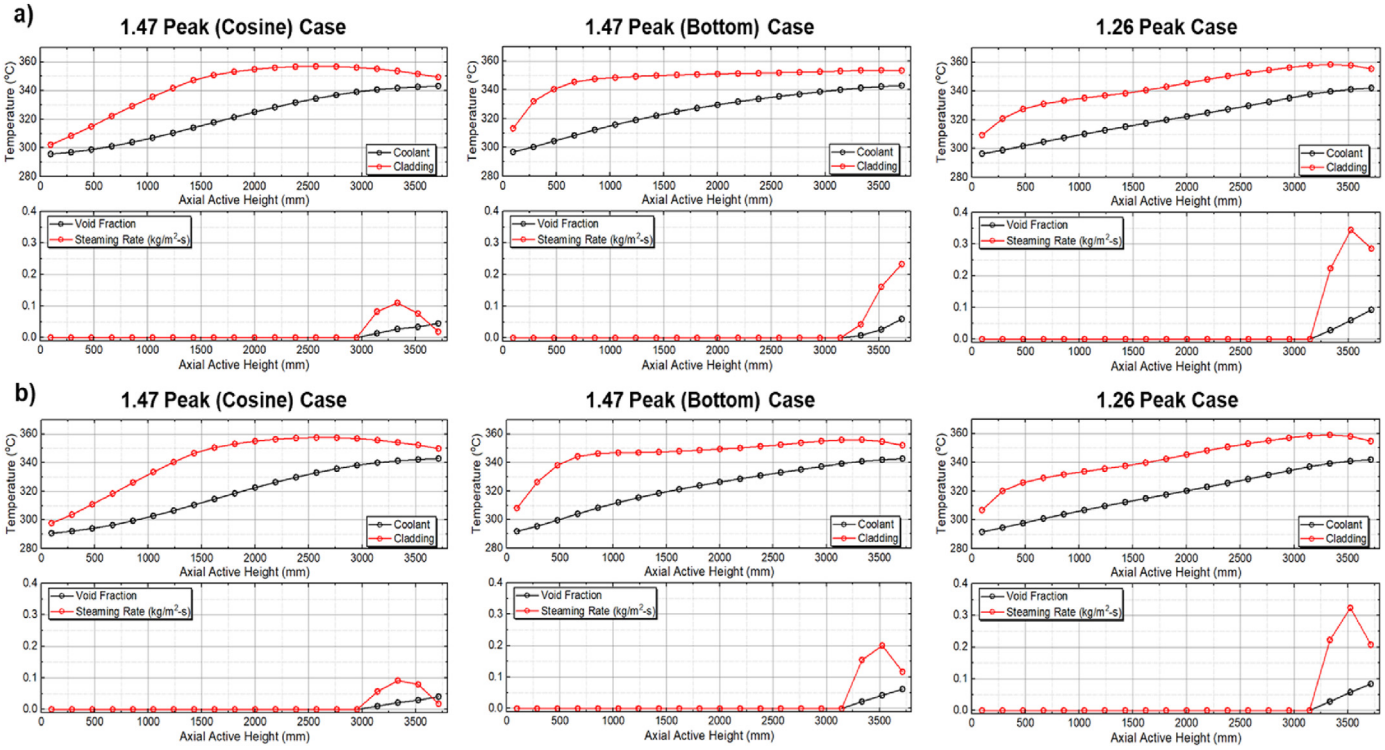

Fig. 11. Hot pin sub-channel analysis results for (a) OPR1000 and (b) APR1400.

Based on the MARS-KS analysis results, the TH conditions of the topmost grid span region (10th grid span) of the hot pin sub-channel, where the vigorous SNB was observed, were chosen as operating conditions of the DISNY test section. The analyzed TH conditions of the topmost grid span region are summarized in Table 2.

The coolant temperature at the inlet of the 10th grid span was ~340 °C regardless of the axial power distribution for both reactor conditions. The space-averaged heat flux in the 10th grid span region was evaluated to be ~600(± 259) kW/m^2. The established TH experimental conditions of DISNY facility for CRUD growth simulation and characterization of CURD fouling resistance are as

Table 2
Summary of MARS-KS hot pin sub-channel 10th grid span region analysis results.

Reactor type	Parameter	1.47 Peak (Cosine) case	1.47 Peak (Bottom) case	1.26 Peak case
OPR1000	**Coolant inlet T**	342.55 °C	342.23 °C	341.17 °C
	Avg. heat flux	368.14 kW/m^2	571.59 kW/m^2	859.32 kW/m^2
APR1400	**Coolant inlet T**	342.21 °C	341.91 °C	340.84 °C
	Avg. heat flux	417.90 kW/m^2	580.30 kW/m^2	854.07 kW/m^2

follows. For the single-phase heat transfer and pressure drop characterization purpose, the inlet temperature conditions of 290 °C, which corresponds to the core inlet conditions, were further considered.

- **Operating pressure**: 155 bar (PWR primary system normal operating condition).
- **Mass flux**: 3300–3,500kg/m^2-s (corresponds to minimum and design mass flux range).
- **Inlet temperature**: 290, 340 °C (corresponds to core inlet and hot pin 10th grid span).
- **Heat flux range**: 0–1,500 kW/m^2 (corresponds to maximum heat flux level of PWR).

3.2. Water chemistry conditions for CRUD growth simulation

The strategy to simulate the CRUD within the DISNY facility was established based on the chemical analysis results of actual PWR. The scanning electron microscopy energy dispersive X-ray spectrometer (SEM-EDS) analysis results of the actual PWR CRUD from Callaway and Korean PWR plants showed that the major component of the PWR is nickel oxide (NiO), nickel ferrite ($NiFe_2O_4$), and zirconium dioxide (ZrO_2) [1,16,33]. In the DISNY facility, Ni and Fe metal ions are used as CRUD precursors to simulate the major components of the CRUD such as nickel oxide and nickel ferrite. The direct injection of Ni and Fe ion method is utilized rather than corrode the structural materials for the easiness of the experiment from the viewpoint of experiment duration time. The Ni and Fe ions are injected into the primary coolant as a form of EDTA (Ethylene diamine tetra acetic acid) [3,20–23,34–36]. The injected Ni/Fe-EDTA are decomposed into Ni and Fe ion in DISNY working conditions [22] and remains as soluble (ion-form) or particulate (metal oxide-form) CRUD sources inside PRS. The Ni/Fe ion ratio in the PRS coolant was set as 2 by considering the composition analysis results of PWR CRUD. The elemental analysis results of PWR CRUDs showed that the ratio of Ni-to-Fe inside the CRUD is almost double. The concentrations of Ni and Fe EDTA inside the PRS coolant are concentrated based on the time ratio between one PWR fuel cycle (~1.5 years) and one week to accelerate the CRUD growth within the day-to-week time framework. The other water chemistry conditions including dissolved oxygen (DO) concentration, dissolved hydrogen (DH) concentration, pH value, and B/Li concentration were set as same with actual PWR conditions.

3.3. Data reduction methodology

The major parameters to quantify the single and two-phase flow heat transfer characteristics of the CRUD deposited cladding surfaces are heat flux (q''), heat transfer coefficient (HTC), the cladding outer temperature (T_o), and the mass flux (G). The heat flux of the HTA heated section was evaluated by Ohm's law as depicted in Eqn. (3). Where, I is the applied electrical current, ΔV_{clad} is the voltage difference across the active heating length, A_{HT} is the effective heat transfer area of HTA, and r_o is the outer radius of cladding respectively. The effective heat transfer area was evaluated by Eqn. (4) and the applied electrical current level was calculated by dividing the measured voltage difference across the shunt resistor by electrical resistance followed by Eqn. (5). Where, L_{clad} is the active heating length of HTA, ΔV_{shunt} is the voltage difference across the shunt resistor, and R_{shunt} is the electrical resistance of shunt resistor respectively.

$$q'' = \frac{I\Delta V_{clad}}{A_{HT}} \tag{3}$$

$$A_{HT} = 2\pi r_o L_{clad} \tag{4}$$

$$I = \Delta V_{shunt}/R_{shunt} \tag{5}$$

The HTCs of the single and two-phase flow are evaluated followed by Eqns. (6) and (7) respectively. For single-phase, HTC is calculated by dividing the heat flux by the temperature difference between the cladding outer temperature and the coolant bulk temperature of the TX heated section (T_{bulk}). For the two-phase, HTC is calculated by dividing the heat flux by the temperature difference between the cladding outer temperature and coolant saturation temperature (T_{sat}). The cladding outer temperature is calculated by Fourier's laws of conduction with a volumetric heat source based on the measured cladding inner wall temperature. The volumetric heat source of the cladding of HTA is evaluated by Eqn. (9). Where $A_{c,clad}$ is the cross-section area of the zirconium-based alloy cladding.

$$h_{SP} = \frac{q''}{T_o - T_{bulk}} \tag{6}$$

$$h_{TP} = \frac{q''}{T_o - T_{sat}} \tag{7}$$

$$T_o = T_i + \frac{q'''}{4k_{clad}}\left(r_i^2 - r_o^2\right) - \frac{q'''}{2k_{clad}} r_i^2 \ln(r_i / r_o) \tag{8}$$

$$q''' = \frac{I\Delta V_{clad}}{A_{c,clad}L_{clad}} = \frac{I\Delta V_{clad}}{\pi\left(r_o^2 - r_i^2\right)L_{clad}} \tag{9}$$

The mass flux (G) of the PRS main piping is calculated by dividing the mass flow rate ($\dot{m}$) with the cross-sectional area ($A_{c,TX}$) of the test section heated channel followed by Eqn. (10). The mass flow rate of the PRS main piping is calculated based on the measured pressure difference across the orifice plate (ΔP_O) and evaluated density of working fluid (ρ_O) followed by Eqn. (11). Where, C_O is the discharge coefficient of orifice plate, D_O is the diameter of the piping, and β is the ratio between the orifice bore diameter and pipe inner diameter. The orifice plate is located upstream region of the preheater, and the density of working fluid is evaluated with measured pressure and temperature values from the measurement instrumentations located downstream region of the orifice flowmeter.

$$G = \frac{\dot{m}}{A_{c,TX}} \tag{10}$$

$$\frac{U_{\dot{m}}}{\dot{m}} = \frac{1}{\dot{m}}\sqrt{\left(\frac{\partial \dot{m}}{\partial C_O}\right)^2 U_{C_o}^2 + \left(\frac{\partial \dot{m}}{\partial D_O}\right)^2 U_{D_o}^2 + \left(\frac{\partial \dot{m}}{\partial \rho_O}\right)^2 U_{\rho_o}^2 + \left(\frac{\partial \dot{m}}{\partial \Delta P_O}\right)^2 U_{\Delta P_O}^2 + \left(\frac{\partial \dot{m}}{\partial \beta}\right)^2 U_{\beta}^2} \tag{16}$$

$$\dot{m} = \frac{\pi}{4} C_O D_O^2 \sqrt{\frac{2\rho_O \Delta P_O}{\left(1-\beta^4\right)}} \tag{11}$$

3.4. Uncertainty analysis

The uncertainty analysis for the key thermal-hydraulic parameters of the DISNY facility was conducted. Table 3 summarizes the measurement uncertainties of the instruments. The uncertainties of heat flux, cladding outer wall temperature, and heat transfer coefficient were calculated by the error propagation method [37] with consideration of 95% confidence interval ranges. The uncertainties of the orifice discharge coefficient, pipe diameter, and the orifice beta ratio are given as 0.88%, 0.3%, and 0.3% respectively. The maximum tolerance error of the radius of the active heater (zircaloy-4 cladding) is assumed as less than 0.2%. The measurement uncertainties of heat flux, cladding outer wall temperature, single/two-phase heat transfer coefficients, and mass flow rate are calculated as given by Eqn. 12–16. The uncertainty values of the heat flux, cladding outer wall temperature, heat transfer coefficients for single/two-phase heat transfer, and mass flow rate are given as ±0.58%, ±1.62%, ±2.28%, ±1.72%, and ±2.16% respectively at 95% confidence level with consideration of coverage factor of 2.

$$\frac{U_{q''}}{q''} = \frac{1}{q''}\sqrt{\left(\frac{\partial q''}{\partial I}\right)^2 U_I^2 + \left(\frac{\partial q''}{\partial \Delta V_{clad}}\right)^2 U_{\Delta V_{clad}}^2 + \left(\frac{\partial q''}{\partial r_o}\right)^2 U_{r_o}^2 + \left(\frac{\partial q''}{\partial L_{clad}}\right)^2 U_{L_{clad}}^2} \tag{12}$$

$$\frac{U_{T_o}}{T_o} = \frac{1}{T_o}\sqrt{\left(\frac{\partial T_o}{\partial T_i}\right)^2 U_{T_i}^2 + \left(\frac{\partial T_o}{\partial q'''}\right)^2 U_{q'''}^2 + \left(\frac{\partial T_o}{\partial r_o}\right)^2 U_{r_o}^2 + \left(\frac{\partial T_o}{\partial r_i}\right)^2 U_{r_i}^2} \tag{13}$$

$$\frac{U_{h_{SP}}}{h_{SP}} = \frac{1}{h_{SP}}\sqrt{\left(\frac{\partial h_{SP}}{\partial q''}\right)^2 U_{q''}^2 + \left(\frac{\partial h_{SP}}{\partial T_o}\right)^2 U_{T_o}^2 + \left(\frac{\partial h_{SP}}{\partial T_{bulk}}\right)^2 U_{T_{bulk}}^2} \tag{14}$$

$$\frac{U_{h_{TP}}}{h_{TP}} = \frac{1}{h_{TP}}\sqrt{\left(\frac{\partial h_{TP}}{\partial q''}\right)^2 U_{q''}^2 + \left(\frac{\partial h_{TP}}{\partial T_o}\right)^2 U_{T_o}^2} \tag{15}$$

3.5. CRUD fouling resistance characterization methodology

In this study, we introduced the concept of fouling resistance widely used in the field of heat exchanger [38–40] to analyze the effects of CRUD deposition on the fuel cladding heat transfer performance. The porous CRUD layer is assumed as the fouling and the corresponding fouling resistance of the CRUD is evaluated by utilizing the 1-D equivalent thermal resistance circuit as proposed by Wang [41]. The 1-D equivalent thermal resistance models for the CRUD fouling resistance evaluation are depicted in Fig. 12. The 1-D thermal resistance network-based approach for evaluating the fouling resistance of CRUD includes the following assumptions. The CRUD layer formed on the cladding surface is assumed to be a simple thermal conduction medium with effective thermal conductivity (k_{eff}) which includes effects of wick boiling phenomena that occur internally. In addition, the difference in heat transfer coefficient (h) on the surface of the heat transfer tube before and after the CRUD deposition is assumed to be negligible. The above-mentioned assumptions used to evaluate the fouling resistance of CRUD have limitations. That may cause distortions of actual physical phenomena such as changes in the surface interfacial heat transfer coefficient due to changes in surface characteristics caused by CRUD deposition. However, it is experimentally very challenging to precisely measure and separate the wick boiling phenomena inside the CRUD layer and the interfacial heat transfer coefficient on the CRUD deposited surface in a high-temperature and high-pressure experimental environment. The thermal resistance of the CRUD derived from this approach is expected to be useful for the modeling of the CRUD thermal resistance with various safety analysis codes.

The two separated thermal resistance circuits for clean, and CRUD-deposited HTA claddings are constructed as shown in Fig. 12 (b) and (c) respectively. The fouling resistance of the CRUD deposit layer is calculated by comparing the heater cladding inner wall temperature difference between clean and CRUD deposited

Table 3
Summary of measurement uncertainties.

Parameter	Instruments	Uncertainties
Temperature	K-type thermocouple	±0.75%
Pressure	Pressure transmitter (Rosemount 2051)	±0.065%
Test section Differential pressure	Differential pressure transmitter (Rosemount 3051)	±0.065%
Orifice flow meter Differential pressure	Differential pressure transmitter (Rosemount 2051)	±0.065%
Voltage difference	Voltage meter (Agilent 34980A)	±0.004%
Electrical current	Shunt resistor (20 μΩ)	±0.04%

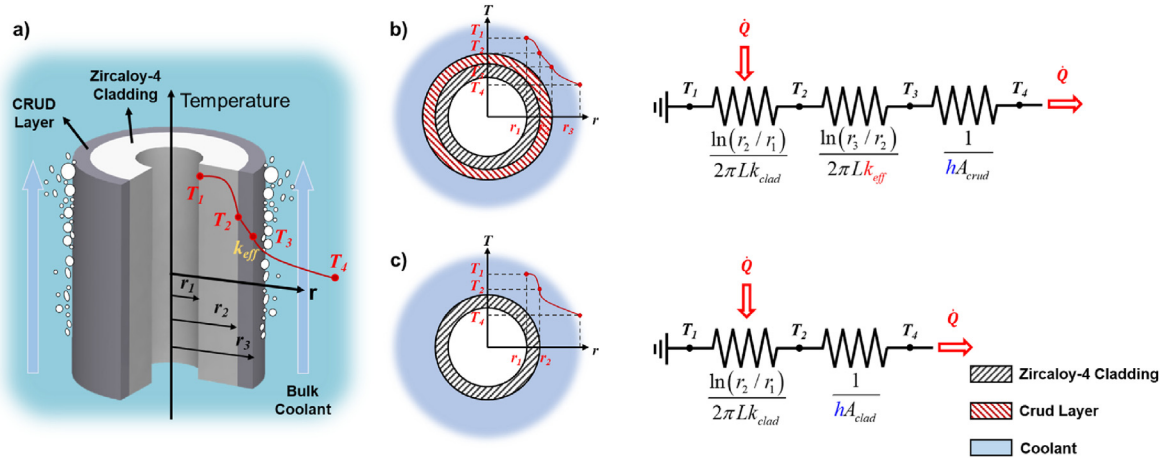

Fig. 12. Explanation on the concept of effective thermal conductivity and equivalent thermal resistance models for the fouling resistance evaluation; (a) schematics on the concept of CRUD effective thermal conductivity under sub-cooled boiling, (b) equivalent thermal resistance circuit of the CRUD deposited cladding, (c) equivalent thermal resistance circuit of the clean cladding.

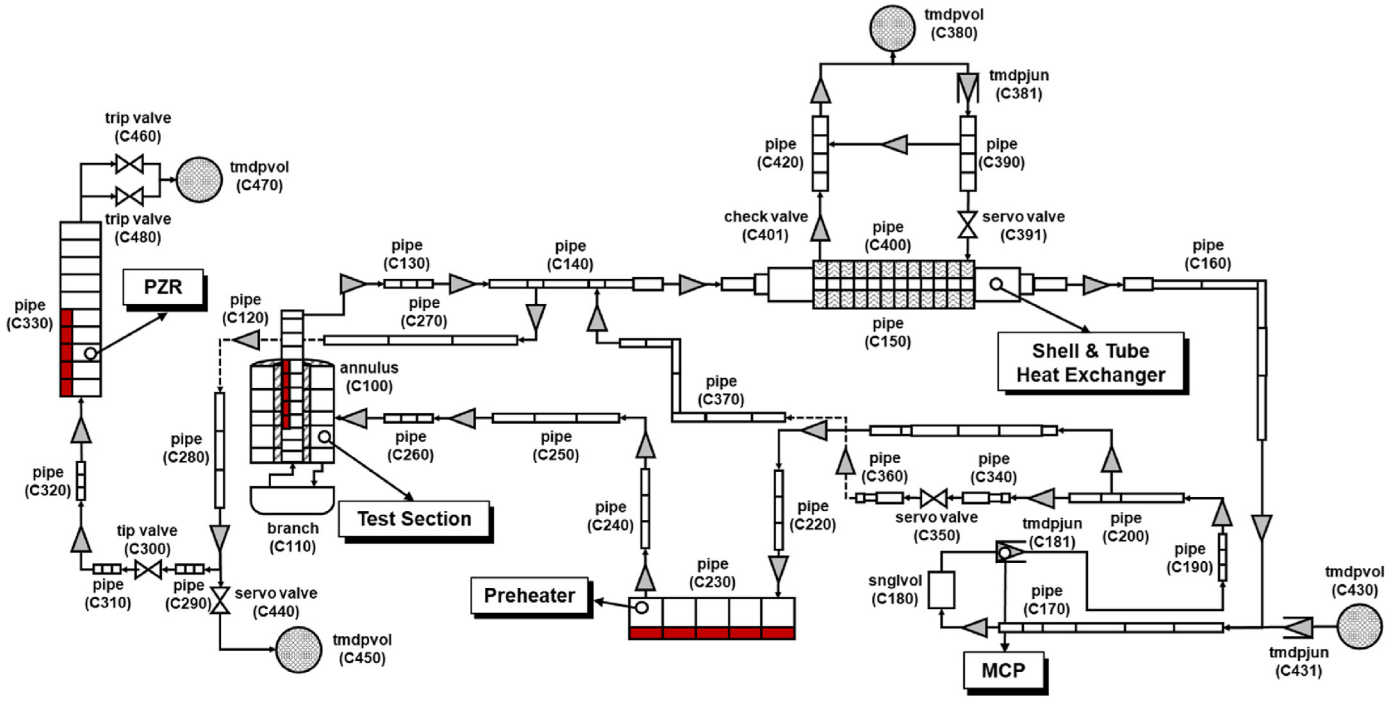

Fig. 13. MARS-KS nodalization of the DISNY for the design feature validation analysis.

cladding under similar TH testing conditions (operating pressure, inlet temperature, mass flux, and applied heat flux). The calculated fouling resistances of the CRUD are quantified as a form of effective thermal conductivity. The effective thermal conductivity of the CRUD is calculated followed by Eqn. (17) based on the sub-cooled flow boiling experimental data before and after the CRUD deposition. Where ΔT is the temperature difference between the heater cladding inner wall and the heated channel bulk fluid.

The effective thermal conductivity includes the effect of the wick boiling (~SNB) inside the porous CRUD and is greatly affected

by the applied heat flux and the flow regime inside the CRUD. The effective thermal conductivity data of simulated CRUD derived from the experimental results of the DISNY device (covering the full heat flux range), can be served as a useful database for evaluating the impact of CRUD deposition on operating power plants.

$$k_{eff} = \frac{q'''\left(r_o^2 - r_i^2\right)(r_o + t_{CRUD})\ln\left(\frac{r_o + t_{CRUD}}{r_o}\right)}{2[(r_o + t_{CRUD})\Delta T_{CRUD} - r_o \Delta T_{Clean}] - t_{CRUD}\left[\left(\frac{q'''}{2k_{clad}}\right)\left(r_o^2 - r_i^2\right) - \left(\frac{q'''}{k_{clad}}\right)\ln\left(\frac{r_o}{r_i}\right)\right]} \quad (17)$$

4. Design validation and verification (V&V) of DISNY facility

4.1. Feasibility analysis of DISNY with MAR-KS code

The design V&V (validation and verification) of the DISNY facility was conducted with the MARS-KS code. The MARS-KS input model of the DISNY facility is shown in Fig. 13. The input model is focused on the PRS side, and the CCS are treated as boundary conditions inside the model.

The main, bypass, and PZR surge piping of the PRS were modeled with pipe components with consideration of form loss coefficient based on the geometrical information. The MCP (C180-181) was modeled as a single volume component with a time-dependent junction component. The tube and shell side of HX was modeled as single pipe components (C150, C400) with the equivalent cross-sectional area and hydraulic diameter. The TX downcomer was modeled as an annulus component (C100), the TX inlet plenum was modeled as a branch component (C110), and TX heated channel was modeled as a pipe component (C120) with proper heat structures to simulate the HTA. The preheater (C230) and PZR (C330) were modeled with pipe components with heat structures to simulate the immersed cartridge heater power during simulation. The air-cooled chiller and CCS was treated as a boundary condition (C380-381; C430, C450, 470) inside the model. The operating conditions (including pressure, temperature, and mass flow rate) of chiller (~5.6 bar; ~100 °C; ~3.4 kg/s) and CCS (~1.7bar-corresponds to 25 cm^3/kg H_2 purging conditions; ~30 °C; ~0.001 kg/s) are assumed as design values. The charging line and letdown line of the DISNY facility was modeled with a time-dependent junction, and servo valves respectively. The steam dump line (C460) and safety relief valves (C480) were modeled as trip valves at the top of the PZR. The heat loss of the DISNY was considered at all the hydraulic components as an HTC boundary condition.

The transition calculation results with MARS-KS are shown in Fig. 14. The V&V calculation with a running time of 150,000s was conducted to confirm the feasibility of DISNY including the start-up, steady-state, and shutdown operations. During the start-up of the DISNY facility, the PRS system pressure increased to 155 bar by PZR immersed heater power. The PZR pressure reaches the operating conditions (155 bar) at ~5.5hr after start-up. After the PRS pressure reach the 155 bar, the working fluid inside the main piping of PRS is heated by preheater operation. The PRS fluid heating is continued until the TX inlet temperature reaches the designated experimental condition (340 °C). The steady-state operating conditions of the DISNY facility were achieved ~13.3hr after the start-up when the TX inlet temperature reach the set point. After the PRS reaches the steady state, the heat flux level of the HTA cladding heater is increased up to 600 kW/m^2 (which corresponds to the CRUD deposition simulation heat flux). The steady state of the PRS is maintained for 10,000 s, without any abnormal situations during the calculation. After the steady state operation, the cooling of the PRS starts. The PRS fluid is cooled down to 80 °C by heat loss of the RPS. The PRS system fluid temperature reaches the cooling set point ~26.0hr after the start-up, and then depressurization of PZR is started. The system pressure is depressurized by PZR heat loss. The system pressure reaches the atmospheric pressure conditions ~33.3hr after the start-up.

The feasibility analysis study with MARS-KS code shows that the DISNY facility can be operated under established experimental conditions ($P = 155$ bar; $T_{in} = 340$ °C) to simulate the CRUD growth under PWR normal operating conditions.

4.2. Performance validation experiments

The performance of the major components such as TX, HTA, PZR, Preheater, and MCP needs to be validated to operate the DISNY facility. Three separate experimental tests were conducted to analyze the performance and functionality of the DISNY facility and corresponding sub-components. The leak-tight or pressurizing test, heat loss test, and single-phase/two-phase heat transfer tests were conducted to validate the performance of the constructed DISNY facility.

4.2.1. Pressurizing and leak-tight test

The pressurizing test of the DISNY facility was conducted to check the validity of the performance of the PZR. The PRS was isolated from the CCS during the pressurizing test. The deionized (DI) water was utilized as a working fluid. After charging the working fluid inside the PRS, the MPC was turned on. The operating pressure of DISNY PRS was increased stepwise way until the system pressure reach ~155 bar by increasing the steam pressure inside the PZR. The transient pressure and water level behavior of the RPS during the pressurizing test are shown in Fig. 15. Where the *PZR-P* is the pressure of PZR, *TX-P* is the test section outlet pressure, and *PMQ-P* is the pressure at downstream of the orifice flow meter. The working fluid temperature inside the PZR and immersed cartridge heater power behavior during pressurizing test are shown in Fig. 16. The *PZR-T-1* is located bottom of the PZR, *PZR-T-2* located middle of the PZR and measures the liquid temperature, and *PZR-T-3* is located top of the PZR and measure the steam temperature respectively.

As shown in Fig. 15, the RPS pressure is increased from 1 bar to 10, 30, 60, 90, 120, and 155 bar. The PRS system pressure reaches the established operating conditions of the DISNY facility 7 h after the starting point of pressuring test. The integrity of the DISNY PRS is secured for 10 h without any leakage or damage while maintaining the system pressure of 153.8 bar. The water level inside the PZR was maintained above 0.4 m which corresponds to the upper limit of the active heating length of the PZR heater heating length during the pressurizing test. The liquid temperature inside the PZR (*PZR-T-3*) was maintained as saturation temperature corresponds to the operating pressure of the PZR with an aid of the PZR-immersed cartridge heater and the bend heater. The power level of

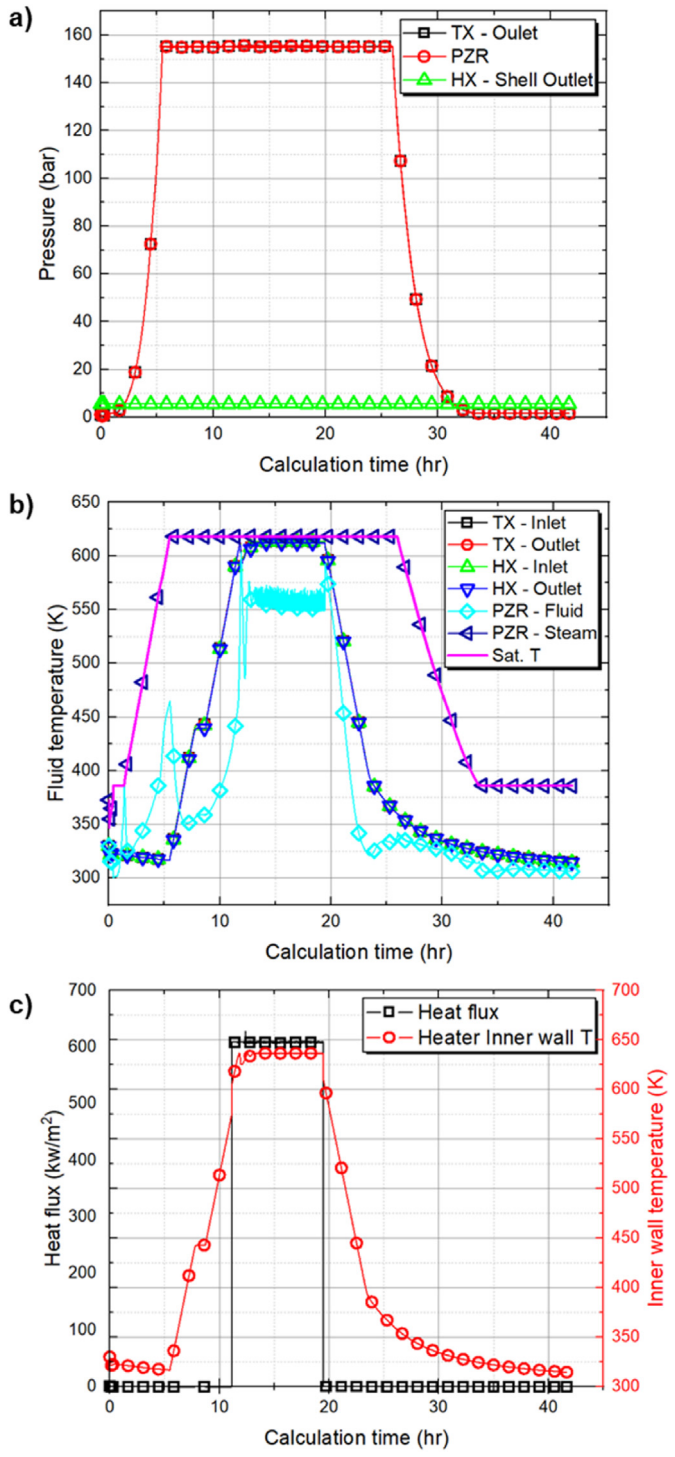

Fig. 14. The feasibility analysis results of the DISNY facility with MARS-KS code; (a) primary and sensitive system pressure, (b) primary system fluid temperature, (c) HTA heat flux and cladding inner wall temperature.

~4.12 kW was applied to the PZR immersed heater to maintain the pressurized states (153.8 bar). The leak-tightness of the DISNY PRS during the pressurizing test was confirmed by an infra-red (IR) camera image. The working fluids temperature was increased up to 150 °C and none of the insulation materials were applied to the major components to inspect the leak-tightness during the pressurizing test. The IR image of the PZR and entire PRS of DISNY are

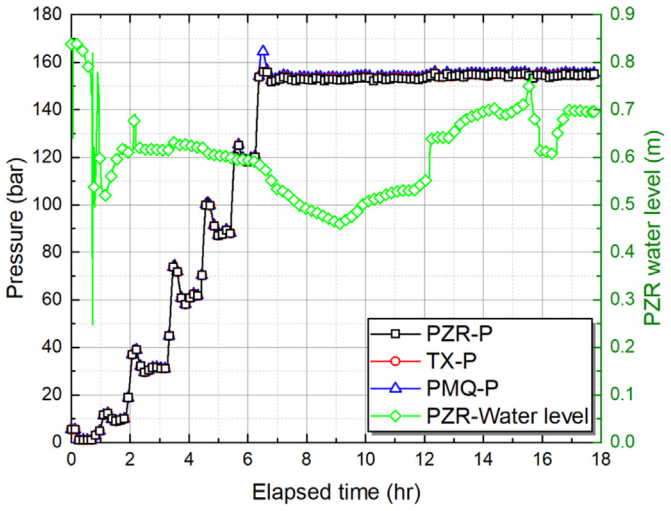

Fig. 15. PRS pressure behavior during the leak tight test of the DISNY facility.

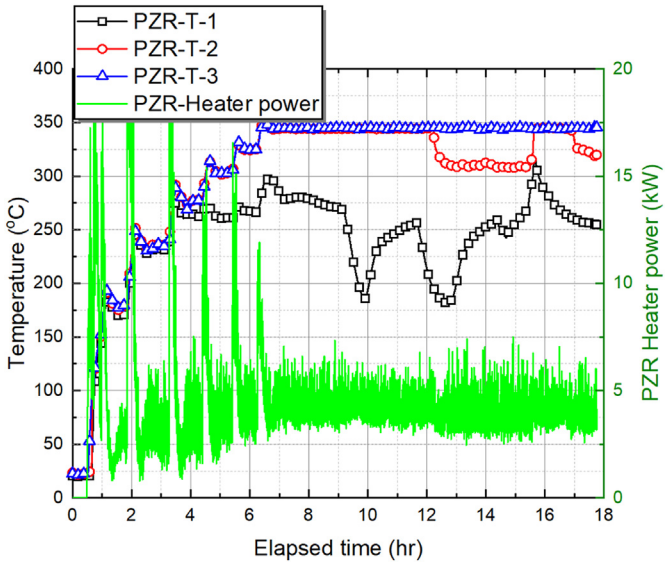

Fig. 16. Working fluid temperature behavior inside the PZR during the leak tight test of the DISNY facility.

shown in Figs. 17 and 18 respectively. Based on the IR camera image, the leak-tightness of the DISNY facility under PWR normal operating pressure condition was validated. The pressuring test result confirms that the constructed DISNY facility can be pressurized up to PWR normal operating pressure conditions while maintaining the system's integrity.

4.2.2. Heat loss test

The heat loss test was conducted to estimate the heat loss characteristics of the DISNY PRS as a function of fluid temperature. The integral approach [42] was utilized to evaluate the heat loss of the PRS by elevating the working fluid temperature stepwise way with the preheater. The preheater power was controlled to maintain the constant PRS temperature distribution. When the PRS temperature distribution became stabilized and reaches a steady state, the supplied preheater power was regarded as heat loss of the PRS of given fluid temperature conditions. The whole PRS of the DISNY was covered with insulating materials during the heat loss test as shown in Fig. 19. The four TCs were attached to the piping

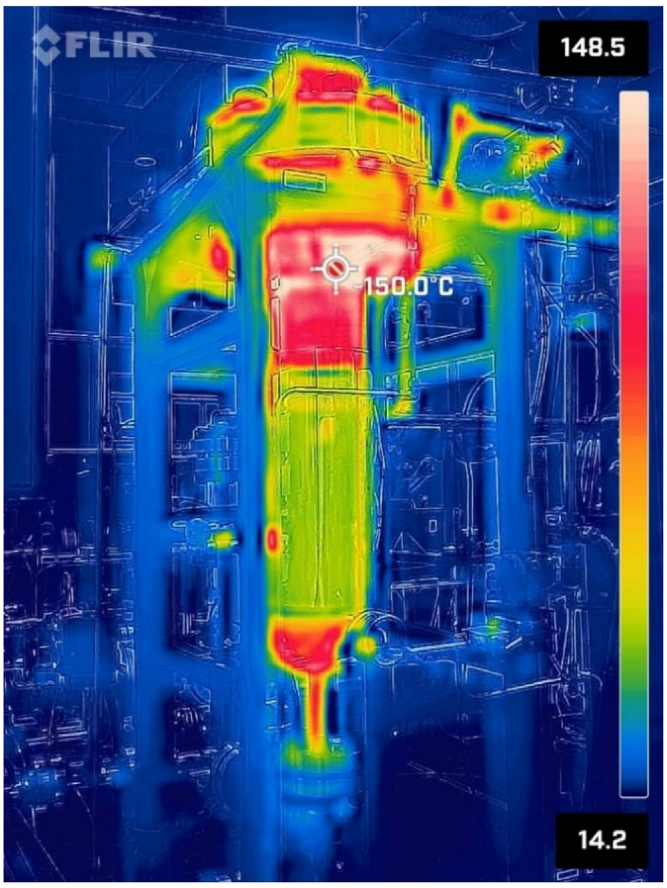

Fig. 17. IR image of the DISNY PZR at $P = 155$ bar operating condition.

walls, which are located between the TX - HX, HX - MCP, MCP - Preheater, and Preheater - TX, to measure the wall temperature distribution of the PRS piping. The PRS working fluid temperature was increased from 30 to 335 °C. The estimated heat loss characteristics of the DISNY PRS along the temperature difference between PRS wall temperature and ambient air are depicted in Fig. 20. As shown in Fig. 20, the heat loss of the PRS increases as the working fluid temperature was elevated and showed exponential

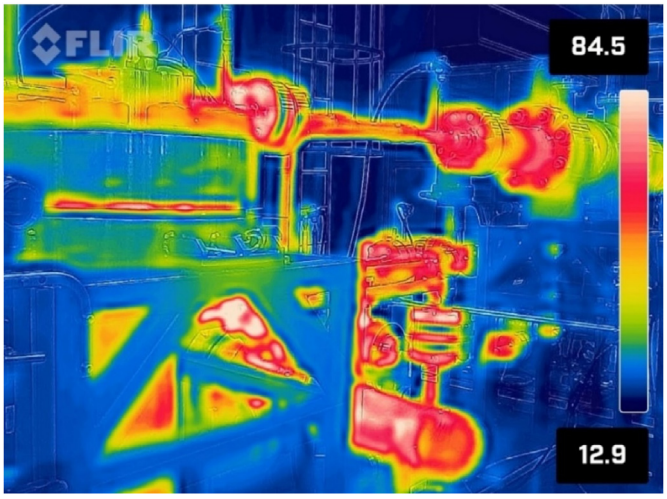

Fig. 18. IR image of the DISNY PRS at $P = 155$ bar, $T = 150$ °C operating condition.

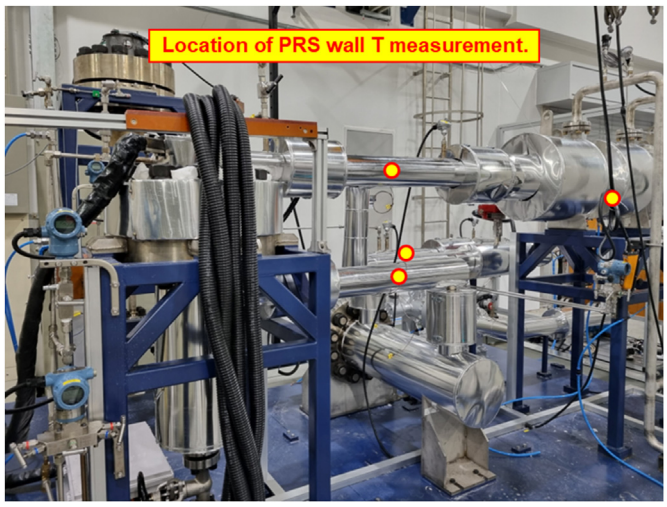

Fig. 19. Photo of DISNY facility with thermal insulation installation.

increasing trends. Based on the experimentally measured heat loss data, following empirical correlation was developed to evaluate the heat loss of the DISNY PRS. Where $Q_{loss,PRS}$ is the amount of heat loss of PRS to the environment, $\overline{T}_w$ is averaged piping wall temperature, and T_{atm} is ambient air temperature.

$$Q_{loss,PRS} = 0.00773(\overline{T}_w - T_{atm})^{5/4} + 8.16E-10(\overline{T}_w - T_{atm})^4 \quad (18)$$

The heat loss characteristic of the given system is affected by the free convection of the ambient air and radiative heat transfer. Therefore, the form of the empirical heat loss correlation takes the superposition of the free convection component and radiation component. It is known that the free convection heat transfer rate of submerged body is proportional to the temperature difference with the power of 5/4 [43]. Therefore, the exponent value in free convection part of correlation is set as 5/4 in the current study. The empirical coefficient values of the proposed heat loss correlation were determined by the data fitting with experimentally measured heat loss data and shows good agreement with R^2 value of 0.97. The heat loss test results reveal that the constructed DISNY facility can

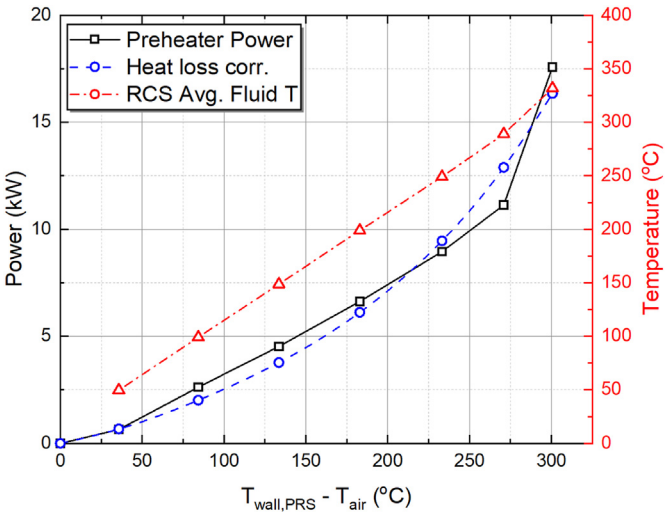

Fig. 20. Evaluated heat loss characteristics of the DISNY PRS.

Table 4
Summary of single and two-phase heat transfer test thermal-hydraulic experimental conditions.

Parameter	Operating P (PZR-P)	TX inlet T (TX-T-2)	Mass Flux (G)	Max. Heat flux
Single-phase HT Test	157.3 (±0.7) bar	291.7 (±2.1) °C	3437.0 (±49.4) kg/m^2-s	1358.8 kW/m^2
Two-phase HT Test	156.6 (±0.4) bar	337.7 (±2.7) °C	3448.2 (±64.8) kg/m^2-s	1349.4 kW/m^2

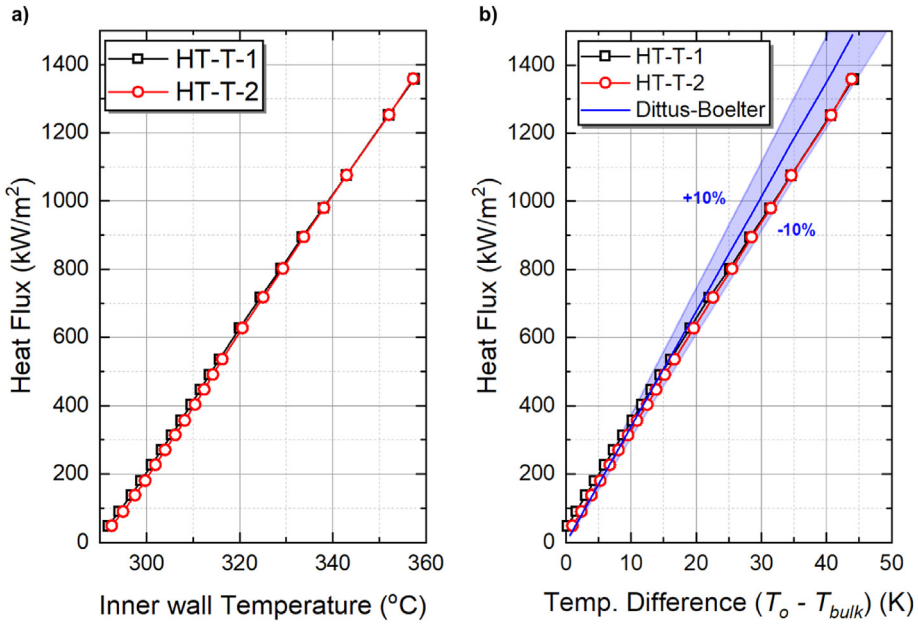

Fig. 21. Single-phase heat transfer experiment results (P = 157 bar; T_{in} = 292 °C; G = 3,437kg/m^2-s); (a) Applied heat flux plotted against measured cladding inner wall temperature; (b) Comparison results with Dittus-Boelter correlation.

increase the working fluid temperature up to the intended design temperature values and shows that the implemented preheater can fully compensate for the heat loss of the PRS under the operational condition.

4.2.3. Single and two-phase heat transfer test

The single and two-phase heat transfer experiments were conducted to validate the performance of the fabricated Joule-heated HTA with TX of the DISNY facility. The validation of HTA's heat transfer performance was performed by comparing the evaluated heat transfer performance with well-established heat transfer correlations. The single-phase and two-phase heat transfer experimental conditions were performed under the TH experimental conditions derived in section 3.1 for simulating CRUD deposition and following fouling resistance evaluation. The experimental conditions for both tests are summarized in Table 4. The applied heat flux level to HTA was increased a stepwise way. When the inner wall cladding temperature (*HT-T-1/2*), TX inlet temperature (*TX-T-1*), and TX mass flux (G) were become stabilized, 40 data points are recorded with 1sec of measuring frequency.

The single-phase heat transfer performance validation test was performed under the thermal-hydraulic test conditions depicted in Table 4. The results of the single-phase heat transfer experiments are described in Fig. 21 (a). The measured inner cladding wall temperature under single-phase flow conditions shows a linearly increasing behavior according to the applied heat flux. The result of calculated the cladding outer wall temperature against the applied heat flux is shown in Fig. 21 (b). For the validation of HTA's single-phase heat transfer performance, comparison between well-known Dittus-Boelter correlation [44] (Eqn. (18)) and single-phase heat transfer results of the HTA was made. Where Re is the Reynolds number of the working fluid inside the TX heated channel, *Pr* is the liquid Prandtl number, and k_l is the thermal conductivity of the working fluid respectively.

$$h_{sp} = 0.023\mathrm{Re}^{0.8}\mathrm{Pr}_l^{0.4}\frac{k_l}{D_h} \tag{18a}$$

As shown in the figure, the single-phase heat transfer performance of HTA in the DISNY device shows good agreement with the Dittus-Boelter correlation within ~10% (based on the HTC). Based on the single-phase heat transfer test results, it was confirmed that the constructed DISNY facility can simulated the single-phase heat transfer performance of the fuel cladding under the PWR reactor operating conditions. Also, the validity of the entrance length of 150 mm considered in the downstream of the heat channel of TX was also confirmed.

The sub-cooled flow boiling (two-phase) heat transfer performance validation test was performed under the thermal-hydraulic test conditions depicted in Table 4. The results of the sub-cooled flow boiling heat transfer experiments are described in Fig. 22 (a). It can be observed that there is a rapid change in the slope of the inner cladding wall temperature increase according to the applied heat flux before and after the heat flux of ~227.1 kW/m^2. This indicates that when the applied heat flux level of HTA exceeds the ~227.1 kW/m2, subcooled nucleate boiling occurred on the surface of the fuel cladding. The onset of nucleate boiling (ONB) on the cladding surface leads to a rapid increase in the heat transfer coefficient between the working fluid and the heated surface. The sub-cooled flow boiling curve of the HTA is shown in Fig. 22 (b). From the sub-cooled flow boiling curve, it was confirmed that the cladding outer wall temperature shows the constant wall superheat

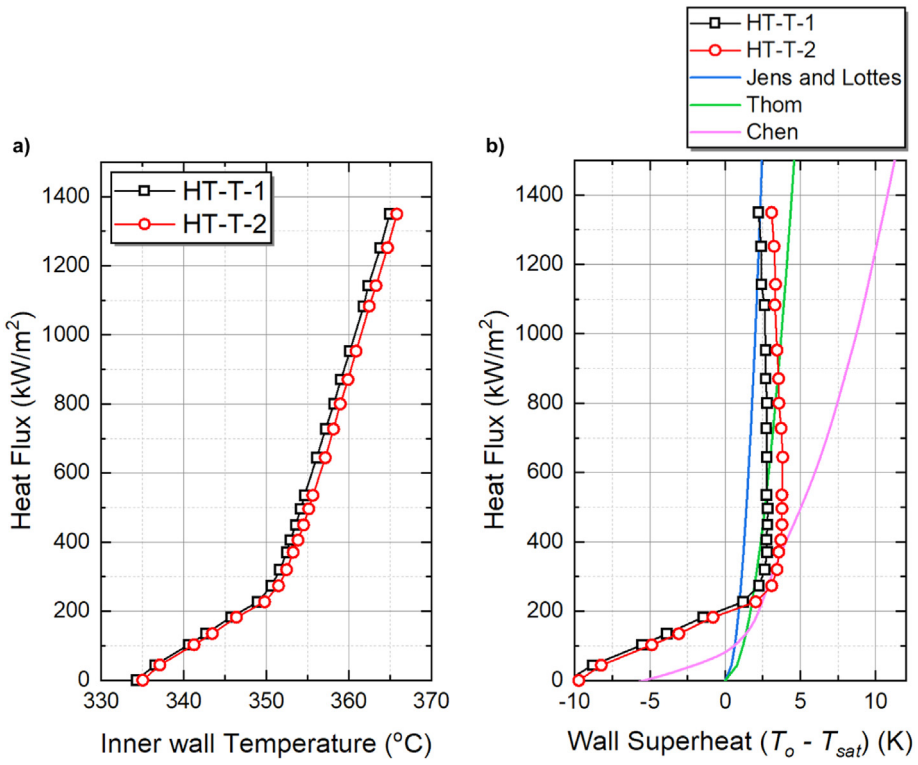

Fig. 22. Two-phase heat transfer experiment results ($P = 157$ bar; $T_{in} = 338$ °C; $G = 3{,}448$kg/m^2-s); (a) Applied heat flux plotted against measured cladding inner wall temperature; (b) Comparison results of boiling curve with sub-cooled flow boiling heat transfer correlations.

of ~3K above the saturation temperature after ONB occurrence. For the validation of HTA's two-phase heat transfer performance, a comparison between sub-cooled flow boiling heat transfer correlations, including Jens and Lottes [45] (Eqn. (19)), Thom [46] (Eqn. (20)), Chen [47] (Eqn. (21)), with the sub-cooled flow boiling curve of the HTA was conducted. Where, P is the operating pressure in MPa, F is the Reynolds number factor, S is the suppression factor, h_{NB} is the nucleate boiling HTC respectively. For the Chen correlation under sub-cooled boiling condition, the F is set equal to unity, the Dittus-Boelter correlation in Eqn. (18) was used to estimate the h_{sp}, and Forster-Zuber correlation [48] in Eqn. (22) was used to estimate the h_{NB}. Where, c_p is the specific heat, σ is the surface tension, μ is the kinematic viscosity, and $P_o - P_{sat}$ is the difference of the saturation pressure corresponding to the wall temperature and saturation temperature respectively.

$$q'' = \left[\frac{\Delta T_{sat}}{25}\exp(P/62)\right]^4 \tag{19}$$

$$q'' = \left[\frac{\Delta T_{sat}}{22.65}\exp(P/87)\right]^2 \tag{20}$$

$$q'' = Fh_{sp}(T_o - T_{bulk}) + Sh_{NB}(T_o - T_{sat}) \tag{21}$$

$$h_{NB} = 0.00122\left[\frac{k_l^{0.79}c_{p,l}^{0.45}\rho_l^{0.49}}{\sigma^{0.5}\mu_l^{0.29}l_{lv}^{0.24}\rho_v^{0.24}}\right](T_o - T_{sat})^{0.25}(P_o - P_{sat})^{0.75} \tag{22}$$

The sub-cooled boiling curve from the DISNY HTA shows the good agreement with the HTC correlation proposed by Jens and Lottes, Thom. The Chen correlation well predict the single-phase heat transfer of the HTA before ONB. However, after the ONB, it over-predicts the wall superheat at given heat flux.

The results of the single and two-phase heat transfer performance validation tests have confirmed that the test section with HTA of the DISNY facility can effectively evaluate the single-phase and two-phase heat transfer in a high-temperature and high-pressure operating conditions of a PWR-type nuclear reactor.

5. Conclusions and future utilization plan of DISNY

The high-pressure subcooled flow boiling experimental facility called DISNY (crud DepoSItion Simulator for Nuclear energY) was designed and constructed as a test bed to analyze the CRUD-related multi-physical phenomena under PWR normal operating conditions. The current experimental facility was designed and constructed to simulate the CRUD under PWR normal operating conditions to establish the CRUD-related experimental database. The detailed system and component design features of the DISNY facility were presented. The thermal-hydraulic and water chemical conditions experimental conditions to simulate PWR CRUD were established based on the hot-pin subchannel analysis and chemical composition analysis of the actual CRUD respectively. The key parameters to quantify the heat transfer performance of the CRUD deposited cladding surface including the fouling resistance was derived and data reduction methodology to evaluate the fouling resistance of the CRUD deposited layer was presented. The performance validation of the DISNY facility and the major sub-components was done by three separate experiments including a leak-tight test, a heat loss test, and a single/two-phase heat transfer test. The feasibility analysis results of the experimental facility based on the MARS-KS calculation show that constructed high-pressure sub-cooled boiling facility can be operated under established experimental conditions to simulate the CRUD growth under PWR conditions.

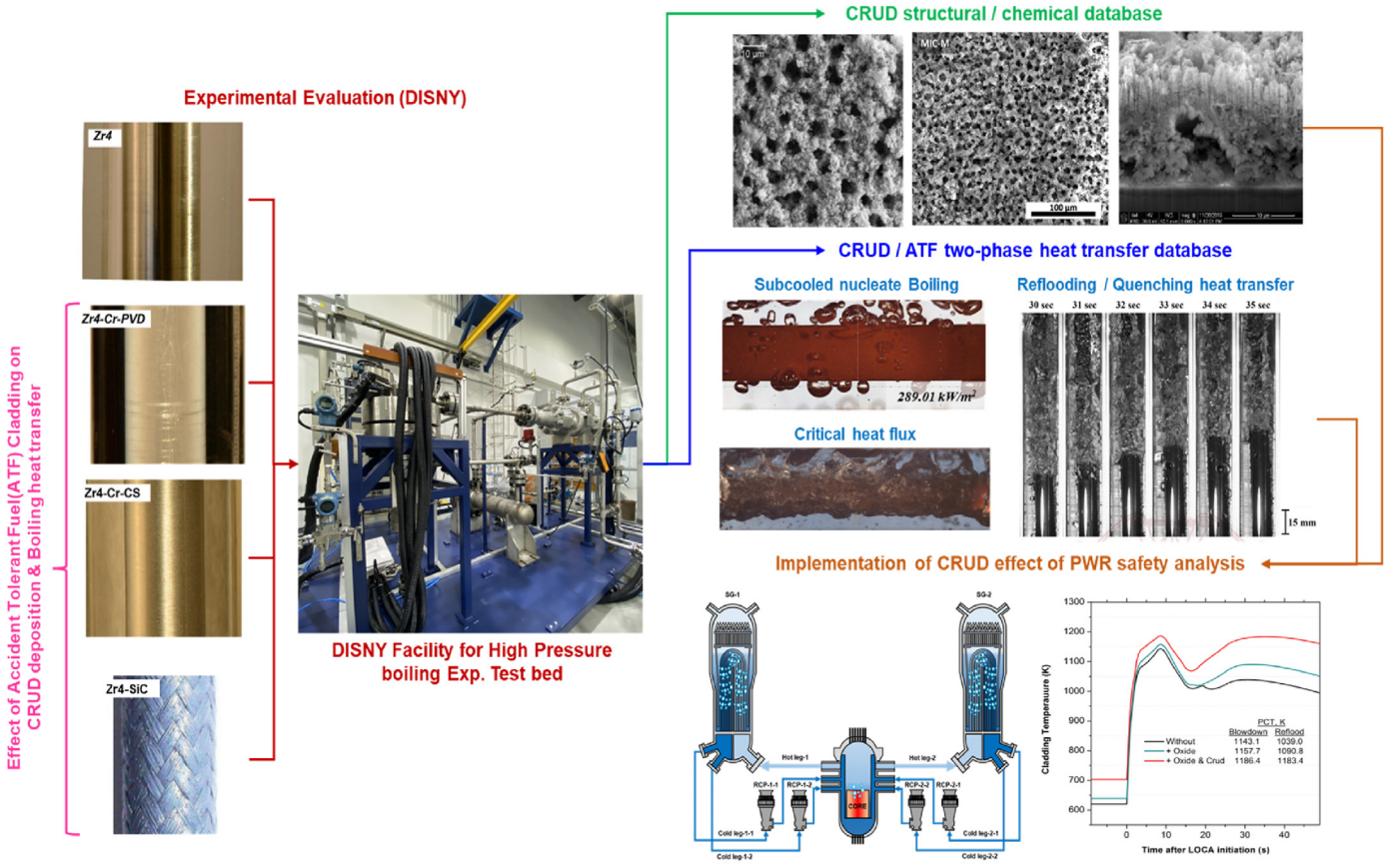

Fig. 23. Schematics on the future utilization plans of the DISNY facility [16,18,49–51].

As a next step, the constructed DISNY facility will be utilized to generate an experimental database of the CRUD deposited cladding's single and two-phase heat transfer characteristics under PWR operating conditions. After the CRUD growth simulation, the chemical composition and surface characteristics, which strongly affect the boiling heat transfer performance, such as surface morphology, wettability, capillarity, and roughness of the simulated CRUD deposited specimen will be quantified. The pool boiling and quenching heat transfer analysis study with CRUD deposited specimen from the DISNY facility are planned to fully understand the effect of the CRUD deposition under the postulated accidental conditions. In addition, the various candidates of accident tolerance fuel cladding including Cr-coating or SiC cladding's CRUD deposition characteristics or the heat transfer characteristics under PWR operating conditions will be analyzed with the DISNY facility. The CRUD database from the DISNY facility is expected to be utilized as a basis for the precise evaluation of the effect of CRUD on PWR safety. The future utilization plans of the DISNY facility are shown in Fig. 23.

Declaration of competing interest

The authors declare that they have no known competing financial interests or personal relationships that could have appeared to influence the work reported in this paper.

Acknowledgement

This work was supported by the Nuclear Safety Research Program through the Korea Foundation Of Nuclear Safety (KoFONS) using the financial resource granted by the Nuclear Safety and Security Commission (NSSC) of the Republic of Korea. (No. 2106022).

Nomenclature

Symbols

A	Area [m^2]
C	Discharge coefficient [−]
c_p	Specific heat [J/kg-K]
F	Reynolds number factor [−]
G	Mass flux [kg/m^2-s]
h	Heat transfer coefficient [W/m^2-K]
I	Electrical current [A]
k	Thermal conductivity [W/m-K]
L	Length [m]
l	Latent heat of vaporization [J/kg]
Q	Heat [W]
P	Pressure [Pa]
p	pitch [m]
q''	Heat flux [W/m^2]
q'''	Volumetric heat source [W/m^3]
R	Electrical resistance [Ω]
r	Radius [m]
S	Suppression factor [−]
s	Steaming rate [kg/m^2-s]
t	Thickness [m]
T	Temperature [^oC]
U	Uncertainty of parameter
V	Voltage [V]

Abbreviations and Acronyms

AOA	Axial offset anomaly
BPR	Back pressure regulator
CCS	Chemical control system
CHF	Critical heat flux
CILC	CRUD induced localized corrosion
CRUD	Chalk river undenied deposit/Corrosion related unidentified deposit
DI	Deionized
FCV	Fluid control valve
HTA	Heater assembly
HTC	Heat transfer coefficient
HX	Heat exchanger
IR	Infra-red
LOCA	Loss of coolant accident
LWR	Light water-cooled reactor
MCP	Main coolant pump
ONB	Onset of nucleate boiling
PRS	Primary system
PWR	Pressurized water reactor
PZR	Pressurizer
RCS	Reactor coolant system
RIA	Reactivity initiated accident
SNB	Subcooled nucleate boiling
TC	Thermocouples
TH	Thermal-hydraulic
TX	Test section

Greek letters

β	Area ratio [−]
Δ	Variance [−]
μ	Kinematic viscosity [N-s/m^2]
ρ	Density [kg/m^3]
σ	Surface tension [N/m]

Subscripts

Atm	Atmospheric condition
bulk	Bulk averaged value
c	Cross section
clad	Cladding
Clean	Clean cladding without CRUD
channel	Flow channel
CRUD	CRUD deposited cladding
eff	Effective
HT	Heat transfer region
i	Inner wall region
l	Liquid phase
loss	Heat loss
lv	Liquid-to-vapor
NB	Nucleate boiling
o	Outer wall region
O	Orifice flow meter
PRS	Primary system
pin	Fuel pin
sat	Saturation state value
shunt	Shunt resistor
v	Vapor phase
wet	Wetted perimeter

References

[1] J.W. Yeon, I.K. Choi, K.K. Park, H.M. Kwon, K. Song, Chemical analysis of fuel crud obtained from Korean nuclear power plants, J. Nucl. Mater. 404 (2010) 160–164, https://doi.org/10.1016/j.jnucmat.2010.07.024.

[2] J. Deshon, Evaluation of Fuel Cladding Corrosion and Corrosion Product Deposits from Callaway Cycle, 14, 2006. Palo Alto, CA, www.epri.com.

[3] G. Wang, A. Byers, M. Young, Simulated Fuel Crud Thermal Conductivity Measurements under Pressurized Water Reactor Conditions, 2011. Palo Alto, CA, www.epri.com.

[4] J. Deshon, D. Hussey, B. Kendrick, J. Mcgurk, J. Secker, M. Short, Pressurized water reactor fuel crud and corrosion modeling, JOM 63 (2011) 64–72. www.tms.org/jom.html.

[5] M.P. Short, D. Hussey, B.K. Kendrick, T.M. Besmann, C.R. Stanek, S. Yip, Multiphysics modeling of porous CRUD deposits in nuclear reactors, J. Nucl. Mater. 443 (2013) 579–587, https://doi.org/10.1016/j.jnucmat.2013.08.014.

[6] P. Cohen, Heat and mass transfer for boiling in porous deposits with chimenys, AlChe Symphsium Series 70 (1972) 71–80.

[7] C. Pan, B.G. Jones, A.J. Machiels, Concentration levels of solutes in porous deposits with chimneys under WICK boiling conditions, Nucl. Eng. Des. 99 (1987) 317–327.

[8] D.Y. Yeo, H.C. No, Modeling heat transfer through chimney-structured porous deposit formed in pressurized water reactors, Int. J. Heat Mass Tran. 108 (2017) 868–879, https://doi.org/10.1016/J.IJHEATMASSTRANSFER.2016.12.046.

[9] J. Henshaw, J.C. McGurk, H.E. Sims, A. Tuson, S. Dickinson, J. Deshon, A model of chemistry and thermal hydraulics in PWR fuel crud deposits, J. Nucl. Mater. 353 (2006) 1–11, https://doi.org/10.1016/J.JNUCMAT.2005.01.028.

[10] I.U. Haq, N. Cinosi, M. Bluck, G. Hewitt, S. Walker, Modelling heat transfer and dissolved species concentrations within PWR crud, Nucl. Eng. Des. 241 (2011) 155–162, https://doi.org/10.1016/J.NUCENGDES.2010.10.018.

[11] N. Cinosi, I. Haq, M. Bluck, S.P. Walker, The effective thermal conductivity of crud and heat transfer from crud-coated PWR fuel, Nucl. Eng. Des. 241 (2011) 792–798, https://doi.org/10.1016/J.NUCENGDES.2010.12.015.

[12] S. Seo, B. Park, S.J. Kim, H.C. Shin, S.J. Lee, M. Lee, S. Choi, BOTANI: high-fidelity multiphysics model for boron chemistry in CRUD deposits, Nucl. Eng. Technol. 53 (2021) 1676–1685, https://doi.org/10.1016/J.NET.2020.11.008.

[13] D.Y. Yeo, H.C. No, Modeling film boiling within chimney-structured porous media and heat pipes, Int. J. Heat Mass Tran. 124 (2018) 576–585, https://doi.org/10.1016/J.IJHEATMASSTRANSFER.2018.03.093.

[14] M. Jin, M. Short, Multiphysics modeling of two-phase film boiling within porous corrosion deposits, J. Comput. Phys. 316 (2016) 504–518, https://doi.org/10.1016/J.JCP.2016.03.013.

[15] P. Saha, N. Aksan, J. Andersen, J. Yan, J.P. Simoneau, L. Leung, F. Bertrand, K. Aoto, H. Kamide, Issues and future direction of thermal-hydraulics research and development in nuclear power reactors, Nucl. Eng. Des. 264 (2013) 3–23, https://doi.org/10.1016/j.nucengdes.2012.07.023.

[16] J. Deshon, PWR Axial Offset Anomaly (AOA) Guidelines, Revision 1, Palo Alto, CA, 2004.

[17] R. Hu, M.S. Kazimi, M.E. Leyse, CONSIDERING THE THERMAL RESISTANCE OF CRUD IN LOCA ANALYSIS, 101, Transaction of the American Nuclear Society, 2009, pp. 590–592.

[18] J. Lee, H. Jeong, Y. Bang, Thermal resistance effects of crud and oxide layers to the safety analysis, in: 2018 TOPFUEL, Prague, Czech Republic, 2018.

[19] I. Dumnernchanvanit, N.Q. Zhang, S. Robertson, A. Delmore, M.B. Carlson, D. Hussey, M.P. Short, Initial experimental evaluation of crud-resistant materials for light water reactors, J. Nucl. Mater. 498 (2018) 1–8, https://doi.org/10.1016/J.JNUCMAT.2017.10.010.

[20] S.H. Baek, H.S. Shim, J.G. Kim, D.H. Hur, Effect of chemical etching of fuel cladding surface on crud deposition behavior in simulated primary water of PWRs at 328 °C, Ann. Nucl. Energy 116 (2018) 69–77, https://doi.org/10.1016/J.ANUCENE.2018.02.030.

[21] S.H. Baek, H.S. Shim, J.G. Kim, D.H. Hur, Effects of heat flux on fuel crud deposition and sub-cooled nucleate boiling in simulated PWR primary water at 13 MPa, Ann. Nucl. Energy 133 (2019) 178–185, https://doi.org/10.1016/J.ANUCENE.2019.05.022.

[22] W.A. Byers, G. Wang, M.Y. Young, J. Deshon, Simulation of PWR crud, in: ICONE22, Prague, Czech Republic, 2014.

[23] G. Wang, W.A. Byers, M.Y. Young, J. Deshon, Z. Karoutas, R.L. Oelrich, Thermal conductivity measurement for simulated PWR crud, in: ICONE21, Chengdu, China, 2013.

[24] Z. Karoutas, G. Wang, W.A. Byers, Critical heat flux and crud WALT loop measurements for westinghouse accident tolerant fuel, in: 2019 TOPFUEL, Seattle, WA, 2019.

[25] R. v Macbeth, R. Trenberth, R.W. Wood, An Investigation into the Effect of "CRUD" Deposits on Surface Temperature, Dry-Out and Pressure Drop, with Forced Convection Boiling of Water at 69 Bar in an Annular Test Section, UKAEA Reactor Group, 1971.

[26] J. Buongiorno, Can corrosion and CRUD actually improve safety margins in LWRs? Ann. Nucl. Energy 63 (2014) 9–21, https://doi.org/10.1016/j.anucene.2013.07.019.

[27] J.Y. Kim, H.J. Kim, I.C. Bang, Design study of CRUD thermal properties characterization facility DISNY under pressurized water reactor normal operating condition, in: Advances in Thermal Hydraulics, ATH 2022), Anaheim, CA, USA, 2022, pp. 563–574, https://doi.org/10.13182/T126-38228.

[28] J.Y. Kim, Y. Lee, J. Ham, J.H. Kim, I.C. Bang, Establishment of experimental facility to investigate the sub-cooled boiling heat transfer characteristics of fouled cladding surface at PWR conditions, The KSFM Journal of Fluid Machinery 25 (2022) 12–21, https://doi.org/10.5293/kfma.2022.25.5.012.

[29] Khnp, Final Safety Analysis Report for Hanbit Unit 5, 6, 1997 (Chapter 4).

[30] Khnp, Final Safety Analysis Report for Shin-Kori Unit 3, 4, 2008 (Chapter 4).

[31] B.A. Khuwaileh, F.I. Al-Hamadi, D. Hartanto, Z. Said, M. Ali, On the performance of nanofluids in APR 1400 PLUS7 assembly: neutronics, Ann. Nucl.

Energy 144 (2020), 107508, https://doi.org/10.1016/J.ANUCENE.2020.107508.
[32] J.-J. Jeong, K.S. Ha, B.D. Chung, W.J. Lee, Development of a multi-dimensional thermal-hydraulic system code, MARS 1.3. 1, Ann. Nucl. Energy 26 (1999) 1611–1642.
[33] J.A. Sawicki, Characterization of Corrosion Products on the Callaway Cycle 9 PWR Core, 2001, https://doi.org/10.13140/2.1.3645.4087. Palo Alto, CA.
[34] J. Ham, Y. Lee, S.C. Yoo, M.P. Short, C.B. Bahn, J.H. Kim, Effect of TiN coating on the fouling behavior of crud on pressurized water reactor fuel cladding, J. Nucl. Mater. 549 (2021), 152870, https://doi.org/10.1016/J.JNUCMAT.2021.152870.
[35] Y. Lee, S.C. Yoo, D. Park, J. Ham, J.H. Kim, Chemistry change of CRUD with various metal ion concentration conditions in PWR fuel cladding, in: 20th International Conference on Environmental Degradation of Materials in Nuclear Power Systems - Water Reactors, Springer, Snowmass Village, CO, USA, 2022.
[36] Y. Lee, J. Ham, D.H. Park, S.C. Yoo, J.H. Kim, Microstructure change of crud with various heat flux conditions, in: PWR FUEL CLADDING, 2021TOPFUEL, Santander, Spain, 2021.
[37] H.W. Coleman, W.G. Steele, Experimentation, Validation, and Uncertainty Analysis for Engineers, John Wiley & Sons, 2018.
[38] M. Awais, A.A. Bhuiyan, Recent advancements in impedance of fouling resistance and particulate depositions in heat exchangers, Int. J. Heat Mass Tran. 141 (2019) 580–603, https://doi.org/10.1016/J.IJHEATMASSTRANSFER.2019.07.011.
[39] A. Fguiri, C. Marvillet, M.R. Jeday, Estimation of fouling resistance in a phosphoric acid/steam heat exchanger using inverse method, Appl. Therm. Eng. 192 (2021), 116935, https://doi.org/10.1016/J.APPLTHERMALENG.2021.116935.
[40] T.L. Bergman, T.L. Bergman, F.P. Incropera, D.P. Dewitt, A.S. Lavine, Fundamentals of Heat and Mass Transfer, John Wiley & Sons, 2011.
[41] G. Wang, Improved CRUD Heat Transfer Model for Dryout on Fuel Pin Surfaces at PWR Operating Conditions, Doctoral thesis, Pennsylvania State University, 2009.
[42] J.B. Lee, Description Report of ATLAS Facility and Instrumentation (Third Revision), Deajeon, Korea, 2020.
[43] J.H. Lienhard, On the commonality of equations for natural convection from immersed bodies, Int. J. Heat Mass Tran. 16 (1973) 2121–2123, https://doi.org/10.1016/0017-9310(73)90116-6.
[44] F.W. Dittus, L.M.K. Boelter, Heat Transfer in Automobile Radiators of Tubular Type, 443–461, 2, Berkeley Univ. California. Publ. Eng., 1930, p. 13.
[45] W.H. Jens, P.A. Lottes, Analysis of Heat Transfer, Burnout, Pressure Drop and Density Date for High-Pressure Water, Argonne National Lab., 1951.
[46] J.R.S. Thom, W.M. Walker, T.A. Fallon, G.F.S. Reising, Boiling in Subcooled Water during Flow up Heated Tubes or Annuli, Paper Presented at the Symposium on Boiling Heat Transfer in Steam Generating Units and Heat Exchangers, Manchester, England. September 15-16, 1965. Cited in JG Collier, Convective Boiling , Cited in JG Collier, Convective Boiling and Condensation. (1972).
[47] J.C. Chen, Correlation for boiling heat transfer to saturated fluids in convective flow, Ind. Eng. Chem. Process Des. Dev. 5 (1966) 322–329.
[48] H.K. Forster, N. Zuber, Dynamics of vapor bubbles and boiling heat transfer, AIChE J. 1 (1955) 531–535.
[49] Youngjae Park, Experimental Study about the Effects of CRUD on Quenching Heat Transfer of Simulated Fuel Rod in Single Flow Channel under PWR Reflood Flow Conditions, Doctoral thesis, Kyunghee University, 2021.
[50] C. Sauder, Ceramic Matrix Composites: Nuclear Applications, Ceramic Matrix Composites: Materials, Modeling and Technology, 2014, pp. 609–646.
[51] D. Lee, B. Elward, P. Brooks, R. Umretiya, J. Rojas, M. Bucci, R.B. Rebak, M. Anderson, Enhanced flow boiling heat transfer on chromium coated zircaloy-4 using cold spray technique for accident tolerant fuel (ATF) materials, Appl. Therm. Eng. 185 (2021), 116347, https://doi.org/10.1016/J.APPLTHERMALENG.2020.116347.